Article

Molecular Cell

RIM and RIM-BP Form Presynaptic Active-Zone-like Condensates via Phase Separation

Graphical Abstract

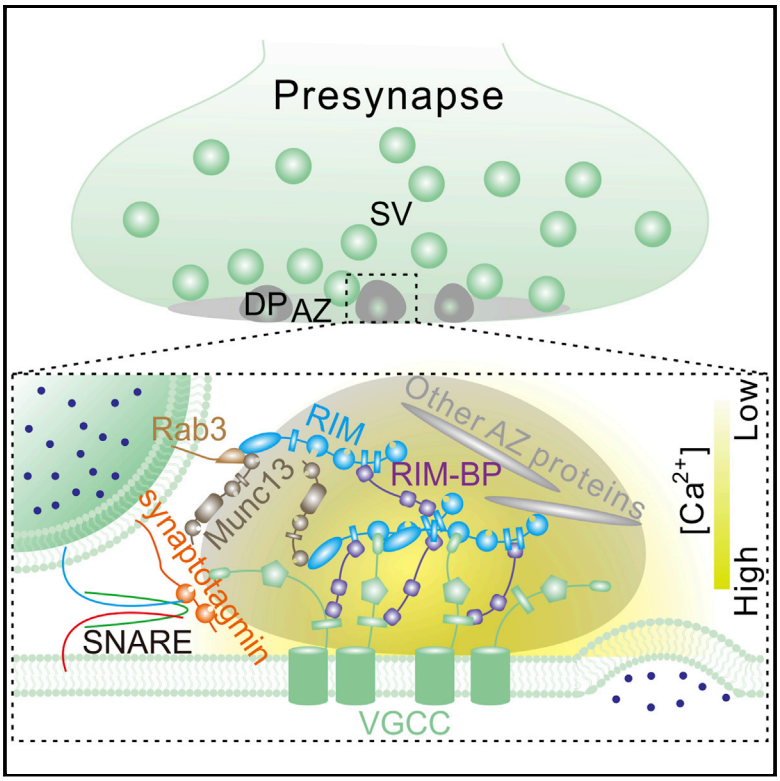

Authors

Xiandeng Wu, Qixu Cai, Zeyu Shen, Xudong Chen, Menglong Zeng, Shengwang Du, Mingjie Zhang

Correspondence

mzhang@ust.hk

In Brief

Clustering of Ca^{2+} channels at presynaptic active zones is critical for precise control of neurotransmitter release. Wu et al. show that the presynaptic active zone scaffold proteins RIM and RIM-BP form self-assembled condensates via liquid-liquid phase separations capable of clustering voltage-gated Ca^{2+} channels on lipid membrane bilayers.

Highlights

- RIM and RIM-BP mixture forms liquid-liquid phase-separation-mediated condensates
- Specific multivalent interaction between RIM and RIM-BP is essential for the LLPS
- RIM and RIM-BP condensates cluster Ca^{2+} channels in solution and on membrane surface
- RIM and RIM-BP are plausible organizers of presynaptic active zones

Wu et al., 2019, Molecular Cell *73*, 1–14
March 7, 2019
https://doi.org/10.1016/j.molcel.2018.12.007

CellPress

Please cite this article in press as: Wu et al., RIM and RIM-BP Form Presynaptic Active-Zone-like Condensates via Phase Separation, Molecular Cell (2018), https://doi.org/10.1016/j.molcel.2018.12.007

Molecular Cell
Article

RIM and RIM-BP Form Presynaptic Active-Zone-like Condensates via Phase Separation

Xiandeng Wu,[1,5] Qixu Cai,[1,5] Zeyu Shen,[1] Xudong Chen,[1] Menglong Zeng,[1] Shengwang Du,[3,4] and Mingjie Zhang[1,2,6,*]
[1]Division of Life Science, State Key Laboratory of Molecular Neuroscience, Hong Kong University of Science and Technology, Clear Water Bay, Kowloon, Hong Kong, China
[2]Center of Systems Biology and Human Health, Hong Kong University of Science and Technology, Clear Water Bay, Kowloon, Hong Kong, China
[3]Department of Physics, Hong Kong University of Science and Technology, Clear Water Bay, Kowloon, Hong Kong, China
[4]Department of Chemical and Biological Engineering, Hong Kong University of Science and Technology, Clear Water Bay, Kowloon, Hong Kong, China
[5]These authors contributed equally
[6]Lead Contact
*Correspondence: mzhang@ust.hk
https://doi.org/10.1016/j.molcel.2018.12.007

SUMMARY

Both the timing and kinetics of neurotransmitter release depend on the positioning of clustered Ca^{2+} channels in active zones to docked synaptic vesicles on presynaptic plasma membranes. However, how active zones form is not known. Here, we show that RIM and RIM-BP, via specific multivalent bindings, form dynamic and condensed assemblies through liquid-liquid phase separation. Voltage-gated Ca^{2+} channels (VGCCs), via C-terminal-tail-mediated direct binding to both RIM and RIM-BP, can be enriched to the RIM and RIM-BP condensates. We further show that RIM and RIM-BP, together with VGCCs, form dense clusters on the supported lipid membrane bilayers via phase separation. Therefore, RIMs and RIM-BPs are plausible organizers of active zones, and the formation of RIM and RIM-BP condensates may cluster VGCCs into nano- or microdomains and position the clustered Ca^{2+} channels with Ca^{2+} sensors on docked vesicles for efficient and precise synaptic transmissions.

INTRODUCTION

Synapses of the CNS are mostly formed by precise juxtaposition of a presynaptic active zone from one neuron with a postsynaptic density from another and are responsible for signal transmissions between neurons. Under an electron microscope, an active zone contains a layer of electron-dense materials beneath the plasma membranes (Couteaux and Pécot-Dechavassine, 1970), and these electron-dense materials are believed to be densely packed proteins (Südhof, 2012). Active zones are known to play critical roles in docking and priming readily releasable synaptic vesicles, clustering and positioning voltage-gated Ca^{2+} channels (VGCCs) at subregions of the presynaptic active zone membrane to regulate both the speed and strength of neurotransmitter release induced by action potentials (Biederer et al., 2017; Südhof, 2012). Electron microscopy (EM) and more recent super-resolution optical microscopic studies, together with electrophysiology experiments, of various neuronal synapses have produced some converged structural properties of active zones, though with difference in certain details. Each active zone typically contains multiple docked vesicles spatially segregated within each bouton (Kaeser et al., 2011; Maschi and Klyachko, 2017; Park et al., 2012; Tang et al., 2016; Watanabe et al., 2013). Correspondingly, VGCCs or their interacting active zone proteins, such as RIM, also form a few clusters instead of being diffusely distributed on an active zone membrane bilayer (Miki et al., 2017; Nakamura et al., 2015; Tang et al., 2016). Both the physical distance of VGCC clusters from the Ca^{2+} sensors at the docked synaptic vesicles and the number of channels in each VGCC cluster are critical determinants of a synapse in interpreting an arriving action potential into both the speed and the amount of transmitters to be released by each nerve pulse (Biederer et al., 2017; Eggermann et al., 2011).

Extensive studies in the past two decades have uncovered a family of scaffold proteins, including RIMs, RIM-BPs, ELKS, liprins, and Munc13s, as key molecular organizers of active zones in connecting VGCCs with the synaptic vesicle fusion machinery (Biederer et al., 2017; Südhof, 2012). Among this set of proteins, RIMs, RIM-BPs, ELKS, and liprins interact with each other, forming a large protein network (Südhof, 2012). VGCCs, via their cytoplasmic tails, are linked to this protein network by directly binding to RIMs and RIM-BPs (Hibino et al., 2002; Kaeser et al., 2011). Munc13s, a very large multi-domain scaffold protein, uses its N-terminal C2A domain to interact with RIMs and its C-terminal MUN domain to bind to the SNARE fusion machinery (Betz et al., 2001; Dulubova et al., 2005; Ma et al., 2011; Richmond et al., 2001; Yang et al., 2015) and thus may function as a linker connecting clustered VGCCs in the active zone with the SNARE fusion machinery.

The dense projections arranged in a grid-like pattern in presynaptic active zones were noticed about half century ago by

Please cite this article in press as: Wu et al., RIM and RIM-BP Form Presynaptic Active-Zone-like Condensates via Phase Separation, Molecular Cell (2018), https://doi.org/10.1016/j.molcel.2018.12.007

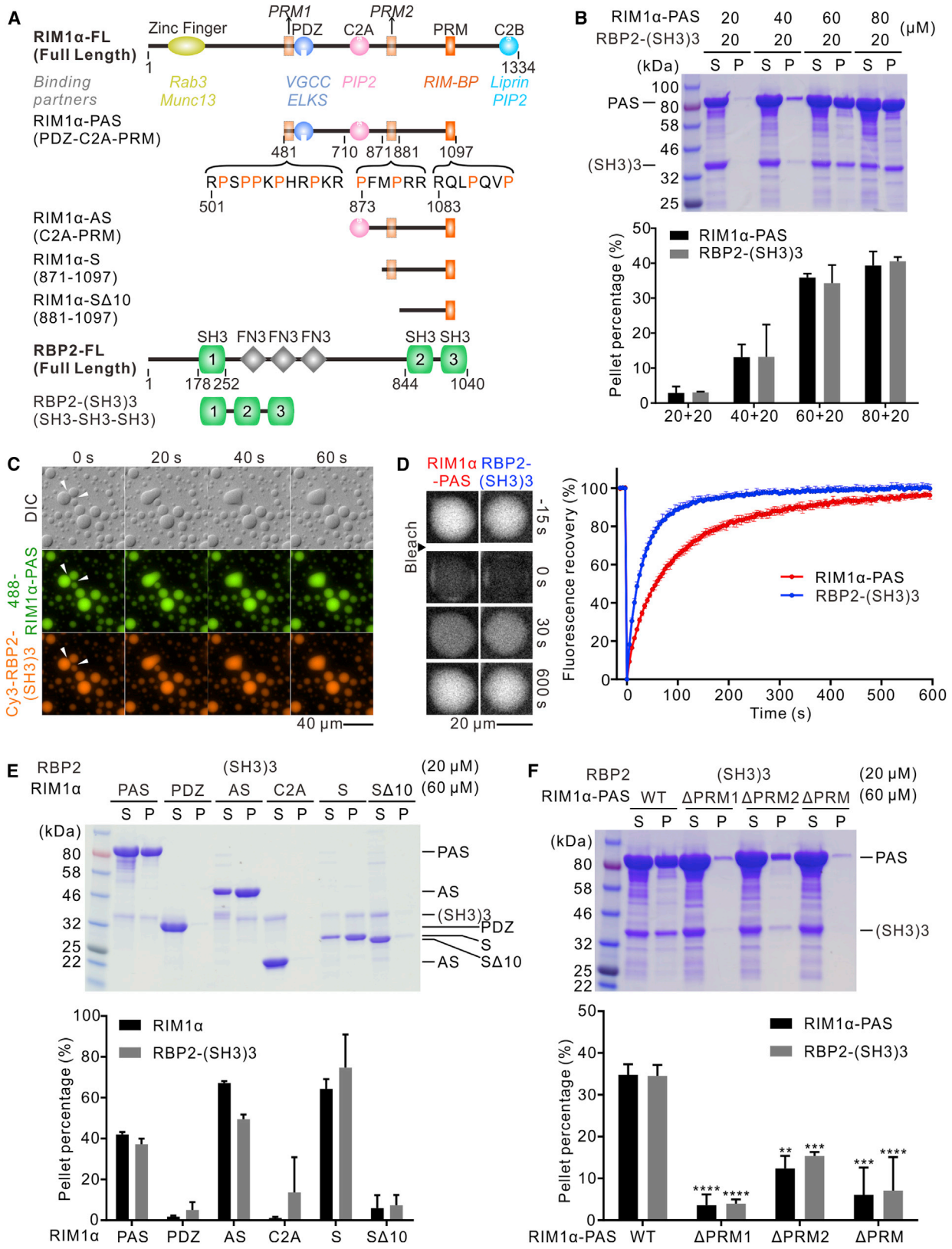

(legend on next page)

EM studies of synapses under chemically fixed conditions (Bloom and Aghajanian, 1966; Gray and Guillery, 1966; Pfenninger et al., 1972), although the molecular components of dense projections remain poorly characterized. The observed dense projections may be an artifact of chemical fixation (Gray, 1975; Siksou et al., 2009; Südhof, 2012), as dense projections have eluded observation by cryo-EM under native conditions. Unlike synaptic vesicles or PSDs, which can be biochemically isolated, dense projections have also escaped biochemical purifications. The elusive nature of dense projections could be due to their unique assembly properties. The fact that dense projections are only visible by EM under chemically fixed samples suggests that the dense projections are metastable and that the condensed molecular assemblies within the dense projections may be easily dispersed once the system is perturbed during biochemical manipulations. Recently, genetic studies have shown that RIMs and RIM-BPs together are critical for the formation of dense projections as well as for essentially all known structural organizations and functions of active zones (Acuna et al., 2016). Another genetic study showed that double knockout of RIM and ELKS disrupted active zone assembly and impaired synaptic transmissions (Wang et al., 2016). Super-resolution imaging studies have also shown that RIMs form dense clusters in active zones (Tang et al., 2016). Thus, RIMs, together with RIM-BPs and/or ELKS, play vital roles in the structural organization of presynaptic active zones. The presynaptic active zones appear to be self-assembled, dynamic protein network structures that are not enclosed by membrane bilayers. However, it remains to be demonstrated whether RIMs and RIM-BPs are sufficient to form active-zone-like structures.

Here, we demonstrate that multivalent interactions between RIM and RIM-BP and their intrinsically disordered properties lead to the formation of self-organized, highly condensed and dynamic assemblies through liquid-liquid phase separation (LLPS) *in vitro*. VGCCs, via direct bindings of their cytoplasmic tails to RIM and RIM-BP, can not only be enriched to the condensed liquid phase, but also significantly promote LLPS of RIM and RIM-BP. Our biochemical reconstitution experiments indicate that RIMs and RIM-BPs are sufficient for forming the dense projection-like structure in presynaptic active zones. Our study also suggests that the RIM and RIM-BP condensates can effectively cluster VGCCs and position clustered VGCCs in close proximity with SNARE fusion machinery for fast and precise synaptic transmission.

RESULTS

RIM1α-PAS and RBP2-(SH3)3 Undergoes Liquid-Liquid Phase Separation *In Vitro*

RIM1α consists of a zinc finger ("Z"), a PDZ (PSD-95, Dlg, ZO-1) domain ("P"), a C2A domain ("A"), a PRM (proline-rich motif; "S" for SH3 domain binding), and a C2B domain ("B") (Figure 1A). As a central organizer in the active zone, RIM can interact with many scaffold proteins and signaling molecules (Figure 1A). The N-terminal zinc finger of RIM binds to Munc13, a very large scaffold protein that assists in vesicle priming (Betz et al., 2001; Dulubova et al., 2005). RIM can tether Ca^{2+} channels to presynaptic active zones through a direct PDZ domain-mediated interaction (Kaeser et al., 2011). The PRM sequence between two C2 domains of RIM can specifically bind to RIM-BP (Wang et al., 2000). The C2B domain forms a weak dimer (Guan et al., 2007) and has direct interaction with liprin and the phospholipid $PI(4,5)P_2$ (de Jong et al., 2018; Schoch et al., 2002). Knockout of RIMs impairs Ca^{2+}-dependent neurotransmitter release and targeting and clustering of Ca^{2+} channels to presynaptic terminals. Expression of RIM1α-PAS fragment can largely rescue the impaired Ca^{2+}-dependent neurotransmitter releases (Kaeser et al., 2011). It was reported that RIM1α-PRM interacts with all three SH3 (Src homology 3) domains of RIM-BP (Wang et al., 2000). Based on the above-mentioned and many additional genetic and cell biology studies in the past, we used purified RIM1α-PAS and the SH3 domains of RIM-BP2 (i.e., by removing the three FN3 [fibronectin type III] domains due to their hitherto unknown functions; Figure 1A) to study their interaction as the starting point.

Individually, both RIM1α-PAS and RBP2-(SH3)3 are soluble monomers in solution in the presence of a moderately high NaCl concentration (200 mM) in the buffer (Figures S1A–S1C), but the solution turns to opalescent once mixed. Using a sedimentation-based assay (Zeng et al., 2016), we found that mixing these two proteins at different molar ratios led to LLPS of both proteins (Figure 1B). The fraction of both proteins recovered

Figure 1. Multivalent Interactions and Intrinsically Disordered Regions Drive the Condensed Phase Formation of the RIM1α-PAS/RBP2-(SH3)3 Mixture

(A) Schematic diagrams showing the domain organizations of RIM1α and RBP2. The sequences of PRM1, PRM2, and PRM are indicated. The figure also shows the binding partners of RIM, the schematic diagrams of various fragments of RIM1α and RIM-BP2, and their abbreviations used in this study.

(B) Representative SDS-PAGE analysis and quantification data showing the distributions of RIM1α-PAS and RBP2-(SH3)3 in the supernatant (S) and pellet (P) in the sedimentation-based assays with the indicated protein concentrations.

(C) Differential interference contrast (DIC) and fluorescence images showing that RIM1α-PAS and RBP2-(SH3)3 were colocalized and enriched in condensed droplets. The droplets that were close to each other were observed to fuse together to generate larger droplets over time (indicated by arrowheads). The concentrations of RIM1α-PAS and RBP2-(SH3)3 were 60 μM and 20 μM, respectively, and 1% of each protein was labeled by the indicated fluorophores.

(D) FRAP experiments showing that fluorescence signals in the condensed phase of both RIM1α-PAS and RBP2-(SH3)3 could near full recovery after photobleaching. The concentrations of RIM1α-PAS and RBP2-(SH3)3 were 60 μM and 20 μM, respectively. Only the protein to be analyzed was Cy3 labeled. The curves represent the averaged signals from 3 droplets with a diameter of ~20 μm. All data are presented as mean ± SD.

(E) Sedimentation-based assays showing LLPS capabilities of various RIM1α fragments (see A for definitions) mixed with RBP2-(SH3)3.

(F) Sedimentation-based assays showing truncation of different PRM regions (PRM1: Δ502–510; PRM2: Δ873–876; PRM: Δ1,086–1,089) weakened or even abolished LLPS of RIM1α-PAS when mixed with RBP2-(SH3)3. For the sedimentation experiments, the fractions of proteins recovered in the condensed phase ("P") were quantified from three independent repeats of the experiment. Statistical data are presented as mean ± SD, with results from 3 independent batches of sedimentation experiments. ns, not significant; *p < 0.05; **p < 0.01; ***p < 0.001; ****p < 0.0001 (one-way ANOVA with Dunnett's multiple comparisons test). See also Figures S1 and S2.

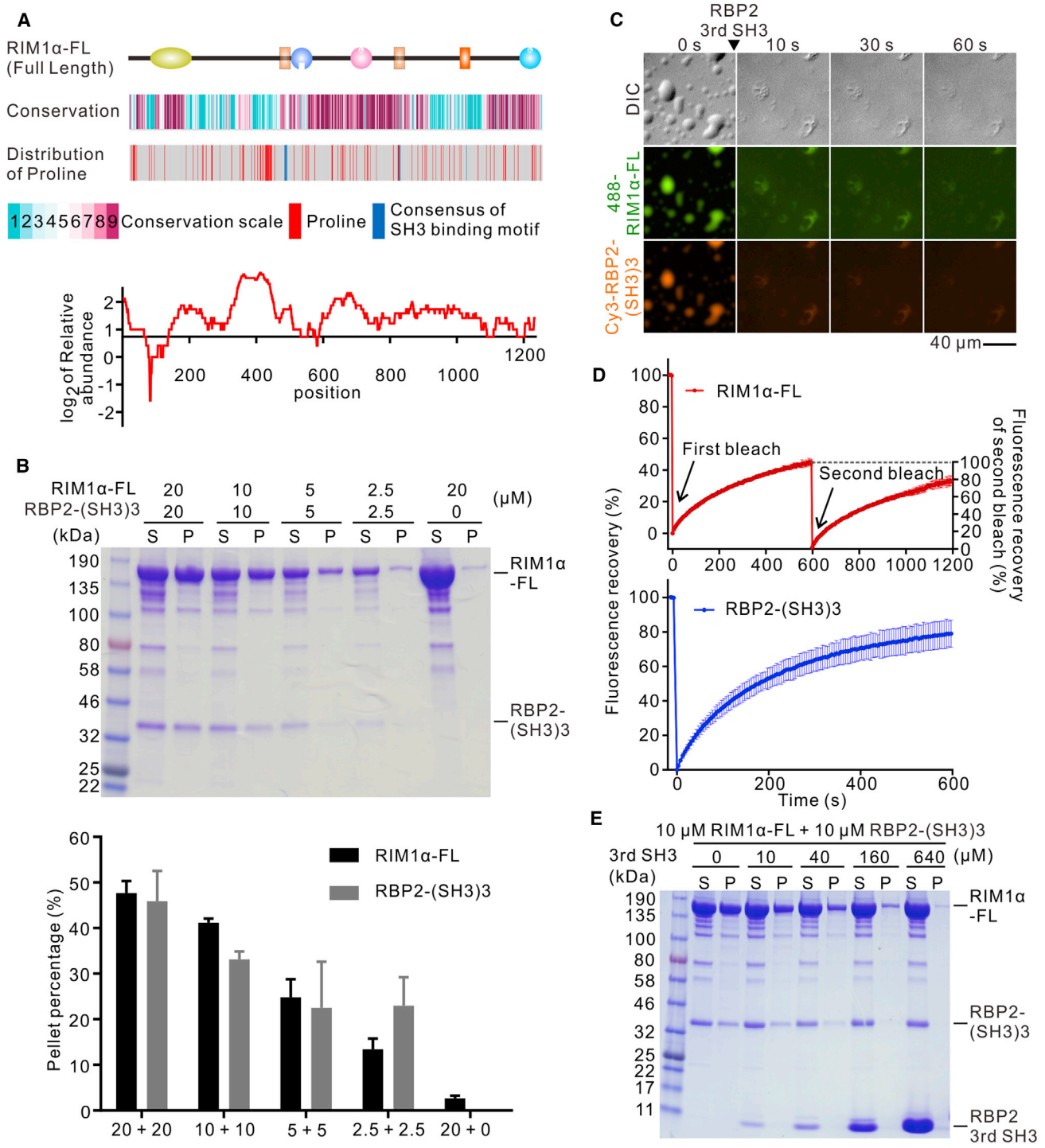

Figure 2. RIM1α-FL Undergoes LLPS with RBP2-(SH3)3 at a Much Lower Threshold Concentration Than RIM1α-PAS Does

(A) Amino acid sequence features of RIM1α. The heatmap below the domain organization diagram shows the amino acid sequence conservation of RIM1α throughout the evolution. The distributions of proline (red) and the consensus SH3-domain-binding motif (RXXPXXP or PXXPXR; blue) of RIM1α are also shown. The abundance of proline distribution of RIM1α was calculated with a 100-residue window and normalized with the average occurrence rate for proline in the vertebrate proteomes to derive the relative abundance values for each position.

(B) Sedimentation-based assays showing the distributions of RIM1α-FL and RBP2-(SH3)3 in the supernatant (S) and pellet (P) when they were mixed at 1:1 molar ratio at the indicated concentrations. The fractions of both proteins recovered in the condensed phase ("P") were quantified from three independent experiments, and the results are expressed as mean ± SD, with results from 3 independent batches of sedimentation experiments.

(legend continued on next page)

from the condensed phase increased when the molar ratios of RIM1α-PAS to RBP2-(SH3)3 increased from 1:1 to 4:1 (the concentration of RBP2-(SH3)3 was fixed at 20 μM in the assay; Figure 1B), presumably due to the presence of multiple SH3 domains of RIM-BP2. We chemically labeled purified RIM1α-PAS and RBP2-(SH3)3 with fluorophores. When mixed, RIM1α-PAS and RBP2-(SH3)3 formed numerous co-localizing spherical droplets, and these droplets are highly enriched with both proteins (Figure 1C). Some of the droplets that were close to each other fused into larger droplets over time (indicated by arrows in Figure 1C). The fluorescence recovery after photobleaching (FRAP) experiment showed that nearly 100% fluorescence intensities were recovered within 5 min for both RIM1α-PAS and RBP2-(SH3)3, indicating that both components could freely diffuse across the boundaries between the condensed phase and diluted phase and exchange with each other without disturbing the concentration difference of the two phases (Figure 1D).

Multivalent Interactions and Intrinsically Disordered Regions Drive the Formation of Condensed Phase by RIM1α-PAS and RBP2-(SH3)3

We then mapped regions of RIM1α responsible for LLPS of the RIM1α-PAS/RBP2-(SH3)3 mixture. An isothermal titration calorimetry (ITC)-based binding assay confirmed the binding between PRM of RIM1α and all three SH3 domains of RIM-BP (Wang et al., 2000) and further showed that the third SH3 domain has the strongest binding affinity (K_d ~1.6 μM; Figures S2A–S2C). However, the valence of the interaction between the single PRM of RIM1α-PAS and the three SH3 domains of RIM-BP2 is unlikely to be sufficient for LLPS of the mixture (Li et al., 2012; Shin and Brangwynne, 2017). We then dissected the regions of RIM1α-PAS that may contribute to the LLPS using a sedimentation-based assay (Figures 1A and 1E). First, removal of a large segment containing the PDZ domain of RIM1α (denoted as "RIM1α-AS" in Figure 1A) did not alter or even slightly increase the LLPS capacity of the RIM1α/RBP2-(SH3)3 mixture. Further removal of the C2A domain ("RIM1α-S" in Figure 1A) also did not alter the LLPS capacity of the RIM1α/RBP2-(SH3)3 mixture. These results indicated that neither PDZ nor C2A of RIM1α is necessary for LLPS of the RIM1α-PAS/RBP2-(SH3)3 mixture. Surprisingly, deletion of 10 residues (aa 871–880) from the N terminus of RIM1α-S (termed RIM1α-SΔ10) nearly abolished its LLPS capability with RBP2-(SH3)3, indicating that this 10-residue fragment (denoted as "PRM2" in Figure 1A) is critical for LLPS. The PRM2 contains a "PFMPRR" sequence, which fits as a class II SH3-binding consensus sequence (Ball et al., 2005). An ITC-based assay showed that the RIM1α PRM2 and a stretch of disordered sequences following PRM2 could indeed bind to RBP2-(SH3)3 (Figures S2E–S2G). Further sequence analysis indicated that another proline-rich sequence immediately preceding the PDZ domain (aa 501–512, termed as "PRM1" in Figure 1A) also belong to the SH3-binding sequence. Deletion of PRM1, PRM2, or PRM greatly weakened LLPS (Figure 1F), indicating that all three PRMs contribute to LLPS. Considering that proline is one of the most abundant residues in intrinsically disordered proteins (Theillet et al., 2013) and the very weak affinities of PRM1 (Figure S2D) and PRM2 in binding to RBP2-(SH3)3, we conclude that both multivalent interaction between RIM1α-PAS and RBP2-(SH3)3 and the intrinsically disordered, proline-rich sequences of RIM1α-PAS are critical for LLPS of the two-protein mixture. Furthermore, there are additional RIM-BP SH3-binding sites in the linker between PRM2 and PRM of RIM (Figure S2G), a region known to be heavily alternatively spliced (Südhof, 2012). It is possible that RIMs with different spliced linkers may have different LLPS capacity and potentially regulate RIM-induced LLPS in the active zone.

We next tested the model of RIM1α-PAS and RBP2-(SH3)3 LLPS via the multivalent interaction between the two proteins. RBP2-(SH3)3 is highly soluble and stays as a monomer at a protein concentration up to 200 μM in the assay condition. We thus performed LLPS experiments by titrating increasing amounts of RBP2-(SH3)3 to a fixed concentration of RIM1α-PAS (60 μM). At a low RBP2-(SH3)3 concentration range (e.g., from 5 μM to 10 μM as shown in the figure), an increase in the RBP2-(SH3)3 concentration promoted LLPS of the RIM1α/RBP2-(SH3)3 complex. A further increase in the concentration of RBP2-(SH3)3 (e.g., from 20 μM to 80 μM) weakened the LLPS of the RIM1α/RBP2-(SH3)3 complex (Figure S1E). This titration experiment indicated that a high concentration of RBP2-(SH3)3 titrated away the large RIM1α/RBP2-(SH3)3 species and thus dispersed the formed RIM1α/RBP2-(SH3)3 droplets, an observation fitting the multivalent protein-protein-interaction-mediated LLPS model (Li et al., 2012). We have also performed a reverse titration experiment by adding increasing concentrations of RIM1α-PAS to a fixed concentration of RBP2-(SH3)3. Since RIM1α by itself could undergo LLPS at high concentrations due to its weak self-association property (Figure S4), increasing the RIM1α-PAS concentration did not obviously disperse RIM1α/RBP2-(SH3)3 droplets (Figure S1D).

RIM1α-FL Undergoes LLPS with RBP2-(SH3)3 at a Much Lower Threshold Concentration than RIM1α-PAS Does

RIM1α is enriched in proline (9.5% for RIM1α; the average occurrence rate for proline in the vertebrate proteomes is ~5%; Figure 2A). The N-terminal 480-residue fragment of RIM, which is not included in RIM1α-PAS, contains two proline-rich regions.

(C) DIC and fluorescence images showing the gradual dispersions of RIM1α-FL and RBP2-(SH3)3 condensed droplets by the addition of the third SH3 domain of RIM-BP2. Both RIM1α-FL and RBP2-(SH3)3 were at 10 μM in the assay.

(D) FRAP experiments showing the recovery curves of the fluorescence signals in the condensed phase of RIM1α-FL and RBP2-(SH3)3 after photobleaching. Only ~50% the fluorescence intensity of RIM1α-FL could be recovered after the first photobleaching, indicating the existence of a less mobile fraction of RIM1α-FL in the condensed phase. The fluorescence intensity of the more mobile fraction of RIM1α-FL could fully recover after the second photobleaching. Both RIM1α-FL and RBP2-(SH3)3 were at 10 μM. Only the protein to be analyzed was Cy3 labeled. The curves represent the averaged signals from 3 droplets with a diameter of ~20 μm. All data are presented as mean ± SD.

(E) Sedimentation-based assay showing that the preformed condensed phase of the RIM1α-FL/RBP2-(SH3)3 mixture could be progressively dispersed by increasing concentrations of the third SH3 domain of RIM-BP2.

See also Figures S3 and S4.

Please cite this article in press as: Wu et al., RIM and RIM-BP Form Presynaptic Active-Zone-like Condensates via Phase Separation, Molecular Cell (2018), https://doi.org/10.1016/j.molcel.2018.12.007

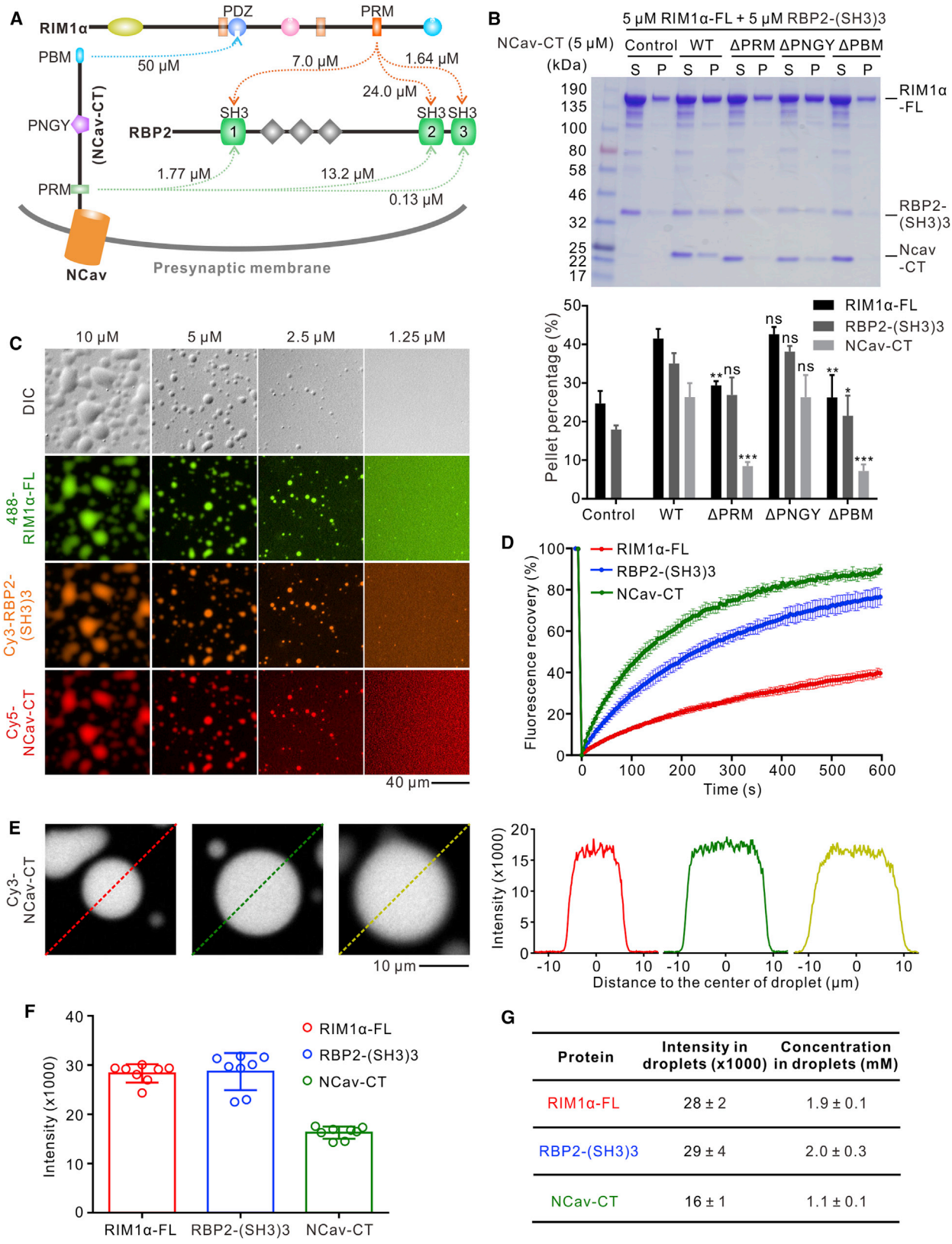

Protein	Intensity in droplets (x1000)	Concentration in droplets (mM)
RIM1α-FL	28 ± 2	1.9 ± 0.1
RBP2-(SH3)3	29 ± 4	2.0 ± 0.3
NCav-CT	16 ± 1	1.1 ± 0.1

(legend on next page)

We further demonstrated that the segment encompassing the two proline-rich regions (aa 183–480), but not the zinc-finger domain, indeed binds to RBP2-(SH3)3, albeit with a relatively weak affinity (Figures S2H–S2J). Therefore, we hypothesized that the full-length RIM (RIM1α-FL) might have a higher capacity for LLPS when mixed with RBP2-(SH3)3. RIM1α-FL could not be expressed and purified using an *E. coli* expression system, probably due to its large size. To overcome this problem, we used a sortase-mediated protein ligation method (Popp and Ploegh, 2011) to link RIM1α-N (aa 1–480, where the last 6 residues were replaced by sortase A recognition sequence "LPETGG") and RIM1α-PASB (aa 481–1,334), both of which could be purified in bacterial expression systems, to obtain RIM1α-FL (Figures S3A and S3B). Purified RIM1α-FL was a monomer in solution and soluble at a concentration up to 50 μM tested, as indicated by a size exclusion chromatography coupled with multi-angle light scattering (SEC-MALS) assay (Figure S3B).

When RIM1α-FL and RBP2-(SH3)3 were mixed at a 1:1 molar ratio, the mixture underwent LLPS at a concentration as low as 2.5 μM (Figure 2B), indicating that the N-terminal proline-rich sequences indeed promote LLPS of RIM1α with RBP2-(SH3)3. We also noted that sub-stoichiometric amount of RBP2-(SH3)3 could efficiently promote LLPS of RIM1α-FL (Figure S3C). We further noted that RIM1α-FL alone at high concentrations could undergo LLPS, and this LLPS was sensitive to the salt concentration in the assay buffer (Figure S4A), indicating that RIM1α-FL has an intrinsic propensity to self-assemble. In the presence of a moderately high concentration of NaCl (300 mM), RIM-FL alone is soluble even at the highest concentration (75 μM) that we tested (Figure S4A). In contrast, even in the presence 300 mM NaCl in the buffer, RIM-FL underwent LLPS at a concentration as low as 5 μM when equal molar ration amount of RBP2-(SH3)3 was added (Figure S3B). In all of the experiments involving RIM-FL in this study, we have included 300 mM of NaCl in the buffer to make sure that RIM-FL does not form LLPS by itself.

DIC and fluorescence image data revealed that both fluorescence-labeled RIM1α-FL and RBP2-(SH3)3 were enriched in condensed droplets (Figure 2C, first column marked with "0 s"; the concentration of each protein is 10 μM). Curiously, the FRAP experiment showed that RIM1α-FL and RBP2-(SH3)3 in condensed droplets had different properties (Figure 2D). Different from the FRAP results of condensed droplets in the RIM1α-PAS/RBP2-(SH3)3 mixture (Figure 1D), less than 50% of the fluorescence intensity of RIM1α-FL could be recovered, indicating the existence of a less mobile fraction of RIM1α-FL in the condensed droplet. A second photobleaching on the same droplet showed that the mobile fraction remained mobile, as the fluorescence intensity could fully recover after the second photobleaching pulse (Figure 2D). The fluorescence intensity of RBP2-(SH3)3 in condensed droplets formed in the RIM1α-FL/RBP2-(SH3)3 mixture could almost fully recover after photobleaching (Figure 2D), suggesting that the immobile fraction of RIM1α-FL in the condensed phase is not an artifact of nonspecific protein precipitation. The smooth fluorescence signal distributions of RIM1α-FL in Figure 2C also indicated that no obvious precipitations exist in the condensed droplets. Both the slower signal recovery rate after photobleaching and the existence of a less mobile fraction of RIM1α may indicate that RIM1α is the key determinant of the formation of RIM1α-FL/RBP2-(SH3)3 condensates.

The third SH3 domain of RIM-BP2 has the strongest binding to PRMs of RIM1α (Figures S2 and 3A). We predicted that the addition of an excess amount of the isolated third SH3 domain of RIM-BP2 to the RIM1α/RBP2 mixture would disperse the condensed phase of the mixture due to disruption of the multivalent interactions between the two proteins. Indeed, injection of the third SH3 domain into a chamber containing condensed droplets formed by RIM1α-FL and RBP2-(SH3)3 led to gradual dispersions of the droplets both by an imaging-based assay (Figure 2C) and by a sedimentation-based assay (Figure 2E). Similarly, adding excess amounts of a synthetic peptide encompassing the PRM sequence of RIM1α could also dissolve the condensed phase formed by RIM1α-FL and RBP2-(SH3)3 (Figure S4C). Taken together, the above results indicate that mixing RIM1α and RIM-BP2 can lead to the formation of self-organized

Figure 3. VGCCs Enrichment in the RIM1α-FL and RBP2-(SH3)3 Condensates

(A) Schematic diagram showing the interaction network of RIM1α, RIM-BP2, and NCav-CT. The binding affinities of each interaction pair were measured by the ITC method (Figures S2 and S5).

(B) Sedimentation-based assays showing NCav-CT could be enriched and in return promote LLPS of RIM1α-FL and RBP2-(SH3)3. The figure also shows that the PRM and PBM, but not the PNGY motif, were critical for NCav-CT's enrichment into the RIM1α-F/RBP2-(SH3)3 condensates. The fractions of all three proteins recovered in the condensed phase ("P") were quantified from three independent experiments. Statistical data are presented as mean ± SD, with data from three independent batches of experiments. ns, not significant; *p < 0.05; **p < 0.01; ***p < 0.001; ****p < 0.0001 using one-way ANOVA with Dunnett's multiple comparisons test.

(C) DIC and fluorescence images showing that NCav-CT was enriched into condensed droplets and colocalized with RIM1α-FL and RBP2-(SH3)3. RIM1α-FL, RBP2-(SH3)3, and NCav-CT were mixed at a 1:1:1 ratio at the indicated concentrations.

(D) FRAP experiments showing the recovery curves of the fluorescence signals of RIM1α-FL, RBP2-(SH3)3, and NCav-CT in the condensed phase after photobleaching. The concentration for all three proteins in this assay was 5 μM. Only the protein to be analyzed was Cy3 labeled. The curves represent the averaged signals from 3 droplets with a diameter of ~20 μm. All data are presented as mean ± SD.

(E) The concentrations of NCav-CT in droplets of different sizes are the same. Confocal images of Cy3-NCav-CT (1% labeled) in condensed droplets formed by RIM1α-FL and RBP2-(SH3)3 are shown on the left. The intensity distributions derived from one representative z-slice completely within the z-dimension of the droplets are shown at right. The starting concentration for all three proteins in the mixture was 10 μM.

(F) Cy3 fluorescence intensity of RIM1α-FL, RBP2-(SH3)3, and NCav-CT in condensed droplets. Data for each protein were collected from 8 droplets in each group and are presented as mean ± SD. The starting concentrations of all three proteins in this assay were 10 μM.

(G) Summary of the fluorescence intensities of each protein as shown in (F) and the corresponding protein concentrations calculated by converting fluorescence intensities to molar concentrations using the calibration curve in Figure S6C. Values are presented as mean ± SD from three independent batches of experiments. See also Figures S2, S5, and S6.

and highly dense structures. The condensed phase formed by RIM1α and RIM-BP2 may act as a platform to recruit other scaffold proteins and signaling proteins, including ELKS, liprins, Munc13, and Rab3/27 in presynaptic termini (Acuna et al., 2016; Südhof, 2012; Wang et al., 2016).

VGCCs Can Not Only Be Enriched But Also Promote LLPS of RIM and RBP

The N-type and P/Q-type VGCCs are known to directly bind to the PDZ domain of RIM (Kaeser et al., 2011) and the SH3 domains of RIM-BP (Hibino et al., 2002) and thus should further increase the valence of the RIM and RIM-BP network (Figure 3A). Thus, we reasoned that VGCCs could be enriched into the condensed phase formed by RIM and RIM-BP, reminiscent of VGCC clustering and channel nano- or micro-domain formation in the presynaptic active zone observed by EM and optical imaging (Nakamura et al., 2015; Tang et al., 2016).

We purified the cytoplasmic tail of the N-type VGCC α1 subunit (termed NCav-CT), which contains three conserved regions: a PRM, a PNGY sequence, and a PDZ binding motif (PBM) (Figure 3A). An ITC-based assay showed that NCav-PRM binds to the three SH3 domains of RIM-BP2 with higher affinities than RIM1α-PRM (Figures 3A and S5A–S5C), and NCav-PBM could indeed bind to RIM1α-PDZ, albeit very weakly (Figures S5D and S5E). Mixing RIM1α-FL, RBP2-(SH3)3, and NCav-CT at a 1:1:1 molar ratio with each protein at 5 μM led to the formation of the condensed phase for all three components. Compared to the control group, which had only RIM1α-FL and RBP2-(SH)3, the addition of NCav-CT not only led to enrichment of NCav-CT to the condensed phase but also promoted LLPS of RIM1α and RIM-BP2 (Figure 3B). Deleting either PRM or PBM from NCav-CT eliminated its enrichment in the condensed phase formed by RIM1α and RIM-BP2, and the degree of RIM1α and RIM-BP2 enrichment in the condensed phase returned to that seen the control group with only RIM1α-FL and RBP2-(SH)3 present in the mixture (Figure 3B). Deletion of the PNGY motif had no impact on condensed phase formation of NCav-CT with RIM1α and RIM-BP2 (Figure 3B). The above results indicate that the multivalent binding of NCav-CT to RIM and RIM-BP is critical for the enrichment of NCav-CT into the condensed phase of the RIM and RIM-BP mixture.

Imaging-based experiments further showed that NCav-CT was enriched into condensed droplets and colocalized with RIM1α-FL and RBP2-(SH3)3 (Figure 3C). The NCav-CT/RIM1α-FL/RBP2-(SH3)3 mixture could undergo phase separation at a concentration as low as 1.25 μM (Figure 3C). FRAP experiments showed that all three components in the condensed phase could exchange with corresponding molecules in the dilute phase. The recovery of RIM1α-FL and RBP2-(SH3)3 was similar to that of the RIM1α-FL and RBP2-(SH3)3 two-component system, and the recovery level of NCav-CT was also very high (Figure 3D).

We next employed a fluorescence-imaging-based assay (Zeng et al., 2018) to measure the absolute concentration of each component in the condensed phase formed by NCav-CT, RIM1α-FL, and RBP2-(SH3)3. In each measurement, only one protein was labeled with Cy3 to avoid potential signal cross-talk between different fluorophores. Images of each droplet were captured by confocal microscopy in the z stack mode with a fixed pinhole size (0.9 μm in this study), and the signal intensities of the confocal layers (i.e., Z-dimension of the point spread functions) that were completely within the height of each droplet were averaged to derive the mean intensity of each droplet (Figures S6A and S6B). The signal intensities of droplets of different size were essentially the same (Figure 3E), indicating that the concentration of each protein in the condensed phase under a given condition is fixed and that increasing the amount of protein leads to larger volumes of the condensed phase but does not change their concentrations. Using a standard curve generated by the known concentrations of single Cy3-labeled proteins in the homogeneous aqueous phase (Figure S6C), we could convert the fluorescence intensities of each protein inside the condensed phase into their absolute concentrations. Strikingly, all the three proteins reached ~1–2 mM concentrations in the condensed phase (Figures 3F and 3G). The sedimentation-assay-based result indicated that ~30%–50% of proteins distributed in the condensed phase (Figure 3B). Assuming that the volume of the condensed phase was negligible for the dilute-phase protein concentration calculations, we could estimate that the concentration in the dilute phase was about half of the initial input (i.e., ~5 μM in this case). This means that formation of the condensed phase enriched NCav-CT, RIM, and RIM-BP by ~200- to 400-fold, demonstrating a role for LLPS in massively concentrating cellular components without the need for any physical barriers, such as membrane bilayers.

NCav-CT Can Be Clustered by RIM and RBP on Supported Lipid Bilayers

N-type and P/Q-type VGCCs are transmembrane proteins specifically enriched in plasma membranes of presynaptic active zones. We next asked whether the formation of the RIM and RIM-BP condensates might be able to cluster VGCCs on membrane bilayers. To test this, we used a supported lipid bilayer (SLB) system that consisted of 98% 1-palmitoyl-2-oleoyl-glycero-3-phosphocholine (POPC), 2% DGS-NTA-Ni^{2+}, and 0.1% PEG5000PE to mimic plasma membranes (Banjade and Rosen, 2014; Zeng et al., 2018) (Figure 4A). We used purified Trx-His_6-NCav-CT for the clustering study, because the His_6 tag in the middle could be used for SLB attachment, and the N-terminal Trx tag was used for fluorophore labeling to avoid nonspecific interactions between the fluorophore and lipid bilayer.

Trx-His_6-NCav-CT alone was evenly distributed (image marked with "0 min" in Figure 4B) and could freely diffuse on the SLB, as indicated by its rapid recovery after photobleaching (Figure S6D). The addition of RIM1α-FL and RBP2-(SH3)3 induced the formation of Trx-His_6-NCav-CT clusters on the SLB within several minutes (Video S1). The clusters of Trx-His_6-NCav-CT progressively grew in size over time (Figure 4B). We labeled RIM1α-FL and RBP2-(SH3)3 with different fluorophores, and confocal images demonstrated that both RIM1α-FL and RBP2-(SH3)3 perfectly colocalized with Trx-His_6-NCav-CT on the SLB (Figure 4C). The clustering patterns of RIM, RIM-BP, and Trx-His_6-NCav-CT on the SLB appeared to be protein-concentration dependent. We coated the membrane with the same amount of Trx-His6-NCav-CT and added different

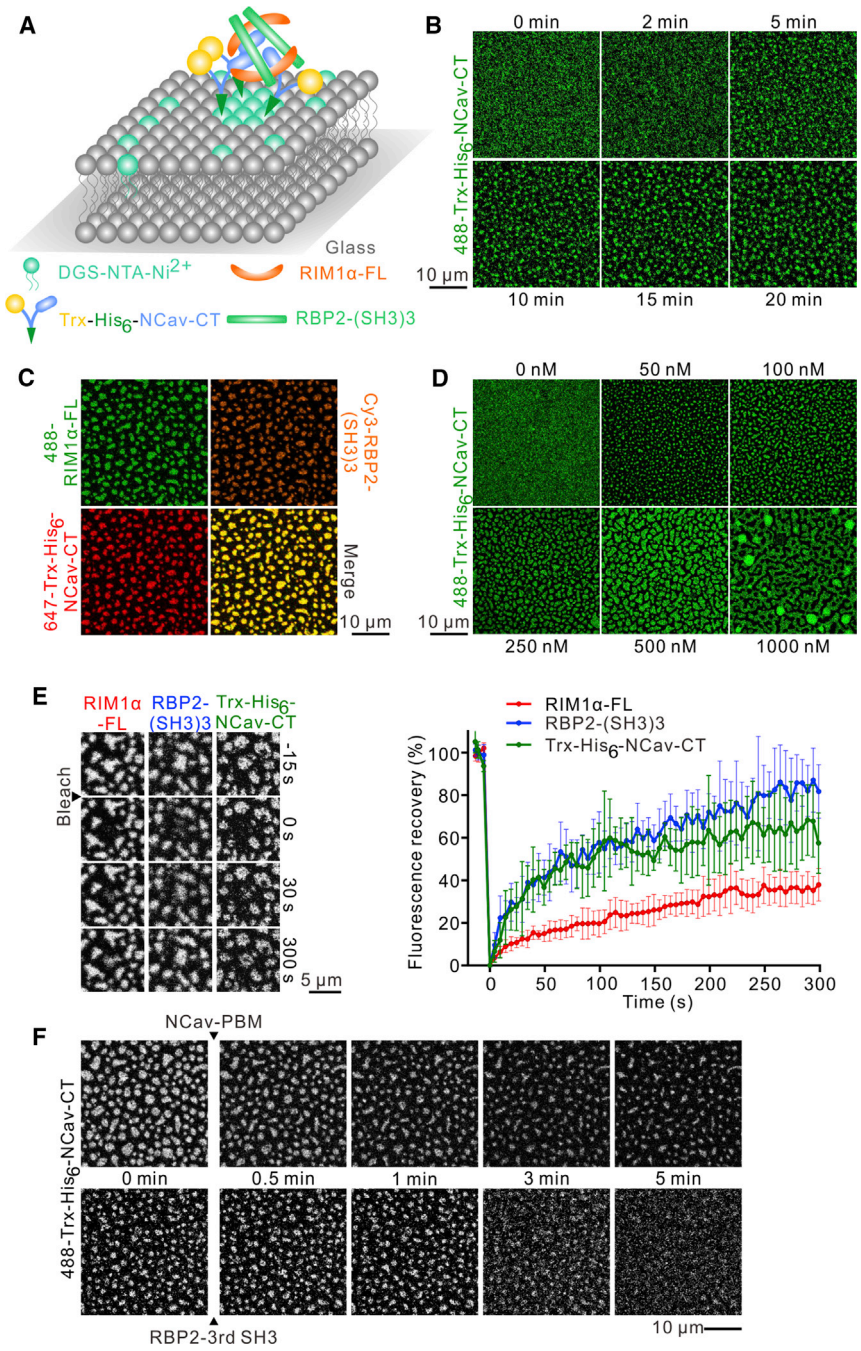

Figure 4. NCav-CT Enrichment in the Condensed Phase Formed by RIM1α-FL and RBP2-(SH3)3 on Membrane Bilayers

(A) Schematic diagram showing clustering of Trx-His_6-NCav-CT on the SLB induced by RIM1α-FL and RBP2-(SH3)3.

(B) Confocal images showing gradual clustering of Trx-His_6-NCav-CT on SLB induced by a very low concentration (100 nM) of RIM1α-FL and RBP2-(SH3)3. See also Video S1.

(C) Confocal images showing the colocalization of RIM1α-FL, RBP2-(SH3)3, and Trx-His_6-NCav-CT in the condensed phase on the SLB.

(D) Different clustering patterns of Trx-His_6-NCav-CT on the SLB induced by increasing concentrations of RIM1α-FL and RBP2-(SH3)3. RIM1α-FL and RBP2-(SH3)3 were mixed at a 1:1 molar ratio at the indicated concentrations.

(E) FRAP assays showing the recovery curves of the fluorescence signals of RIM1α-FL, RBP2-(SH3)3 and NCav-CT in the condensed phase on the SLB after photobleaching. The FRAP curves represent averaged results from 5 bleached regions with a squared-shape size of 4 μm^2. Data are presented as mean ± SD.

(F) Confocal images showing the gradual dispersions of Trx-His_6-NCav-CT clusters on the SLB by the addition of NCav-PBM (top row) or the third SH3 domain of RIM-BP2 (bottom row). The concentration of RIM1α-FL and RBP2-(SH3)3 is 100 nM. See also Video S2.

See also Figure S6.

concentrations of the RIM1α-FL/RBP2-(SH3)3 mixture fixed at a 1:1 molar ratio. At the lowest 50 nM concentration tested, the clusters of Trx-His6-NCav-CT were all very small in size. The sizes of the clusters continued to become larger when concentrations of RIM1α-FL and RBP2-(SH3)3 added were increased (Figure 4D), consistent with the theory of phase transitions. When the concentration of the RIM1α-FL/RBP2-(SH3)3 mixture reached 1,000 nM, the clusters became a mesh-like structure spanning entire field. In spite of different morphologies at different RIM1α-FL/RBP2-(SH3)3 concentration groups, all the clusters were evenly distributed, suggesting that the phase separation of the Trx-His_6-NCav-CT/RIM1α-FL/RBP2-(SH3)3 on the SLB followed a spinodal decomposition mode (e.g., at the 1,000 nM RIM1α-FL/RBP2-(SH3)3 concentration) or a combination of spinodal decomposition and binodal nucleation modes at lower protein concentrations (Banjade and Rosen, 2014; Berry et al., 2018; Zeng et al., 2018). It is also noted that the threshold concentration for Trx-His_6-NCav-CT/RIM1α-FL/RBP2-(SH3)3 on the SLB to undergo LLPS can be as low as 50–100 nM (Figure 4D), matching the physiological concentration of RIM and RIM-BP in each presynaptic bouton estimated by quantitative proteomic methods (Wilhelm et al., 2014). FRAP experiments showed that molecules between the condensed phase and the dilute phase on the SLB underwent dynamic exchanges (Figure 4E).

It is known that the interaction between NCav-PBM and RIM-PDZ, though with a very weak affinity, is critical for targeting and clustering NCav at presynaptic termini (Kaeser et al., 2011). We tested whether a synthetic NCav-PBM peptide could disperse Trx-His6-NCav-CT clusters on the SLB by competing for binding to the PDZ domain in RIM1α-FL. Indeed, the addition

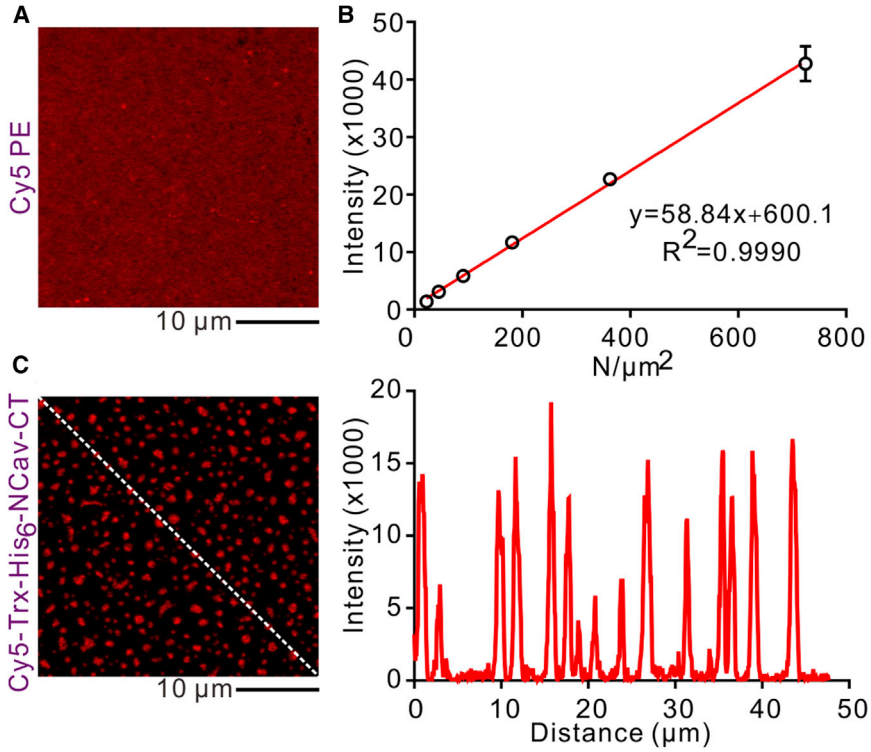

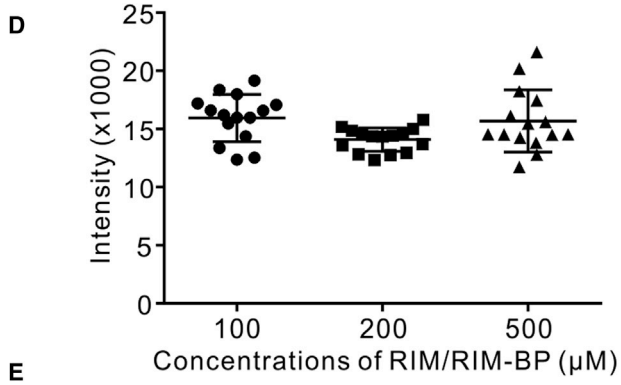

E

Intensity in clusters (x1000)	14 ± 1
Cy5 density in clusters (N/μm^2)	228 ± 7
NCav-CT density in clusters (N/μm^2)	11,400 ± 350

Figure 5. Estimation of Absolute NCav-CT Density on the SLB

(A) Representative confocal image of SLB with (1/4)% Cy5 PE. Cy5 PE was evenly distributed on the SLB.

(B) A standard curve showing fluorescence intensity versus Cy5 density. Six images were captured and analyzed for each data point, and data are presented as mean ± SD.

(C) Representative confocal image of 2%-Cy5-labeled Trx-His$_6$-NCav-CT on the SLB after clustering induced by 200 nM unlabeled RIM1α-FL and RBP2-(SH3)3. The right panel is a line-plot of the Cy5-labeled Trx-His$_6$-NCav-CT intensities of the dashed line in the left panel.

(D) Mean fluorescence intensities of Cy5-labeled Trx-His$_6$-NCav-CT derived from 15 clusters randomly chosen from five different images of each condition.

(E) Absolute density of Trx-His$_6$-NCav-CT was calculated using the standard curve shown in (B). Data are presented as mean ± SD from three independent batches of experiments.

of NCav-PBM led to gradual dispersion of preformed Trx-His$_6$-NCav-CT clusters (Figure 4F, top panel). Similarly, the addition of RBP2-3rd SH3 also disrupted preformed Trx-His$_6$-NCav-CT clusters and with a higher efficiency than NCav-PBM (Figure 4F, bottom panel; also see Video S2), likely due to the very-high-affinity binding of the SH3 domain to NCaV PRM (K_d ~0.13 μM, Figures 3A and S5C).

We next measured the density of Trx-His$_6$-NCav-CT in the condensed phase on the SLB. At a given initial density of Trx-His$_6$-NCav-CT (~1,190 molecules/μm^2 in this case), the fluorescence intensities (and therefore the density) of Cy5-Trx-His$_6$-NCav-CT inside the clusters remained constant regardless the amount of RIM1α-FL and RBP2-(SH3)3 added to the SLB system (Figure 5D). This finding is consistent with the fluorescence intensity measurement of the NCav-CT/RIM1α-FL/RBP2-(SH3)3 droplets in solution shown in Figures 3E–3G. By the standard curve generated using Cy5-labeled 1,2-dioleoyl-sn-glycero-3-phosphoethanolamine (PE) (Figures 5A–5C), the density of the cluster Trx-His$_6$-NCav-CT on the SLB was calculated as ~11,400 molecules/μm^2 (Figure 5E).

We next tested the specificity of Trx-His$_6$-NCav-CT on the SLB by the RIM1α-FL/RBP2-(SH3)3 complex. We showed that RBP2-(SH3)3 alone could not induce the clustering of Trx-His$_6$-NCav-CT on the SLB (Figure S6E), suggesting that RIM and RIM-BP together induce clustering of the channel. We also used PSD95 and SynGAP (Zeng et al., 2016), two postsynaptic scaffold proteins containing both PDZ and SH3 domains, to test whether these two unrelated proteins may cluster Trx-His$_6$-NCav-CT on SLB. The C-terminal half of SynGAP (containing the coiled-coil domain followed by a PBM, denoted as "CC-PBM") and Alexa-Fluor-647-labeled PSD95 were sequentially added to the SLB coated with Trx-His$_6$-NCav-CT. The fluorescence images showed that Trx-His$_6$-NCav-CT was still evenly distributed on the SLB, even when added PSD95 and SynGAP formed condensed droplets via LLPS (Figure S6F).

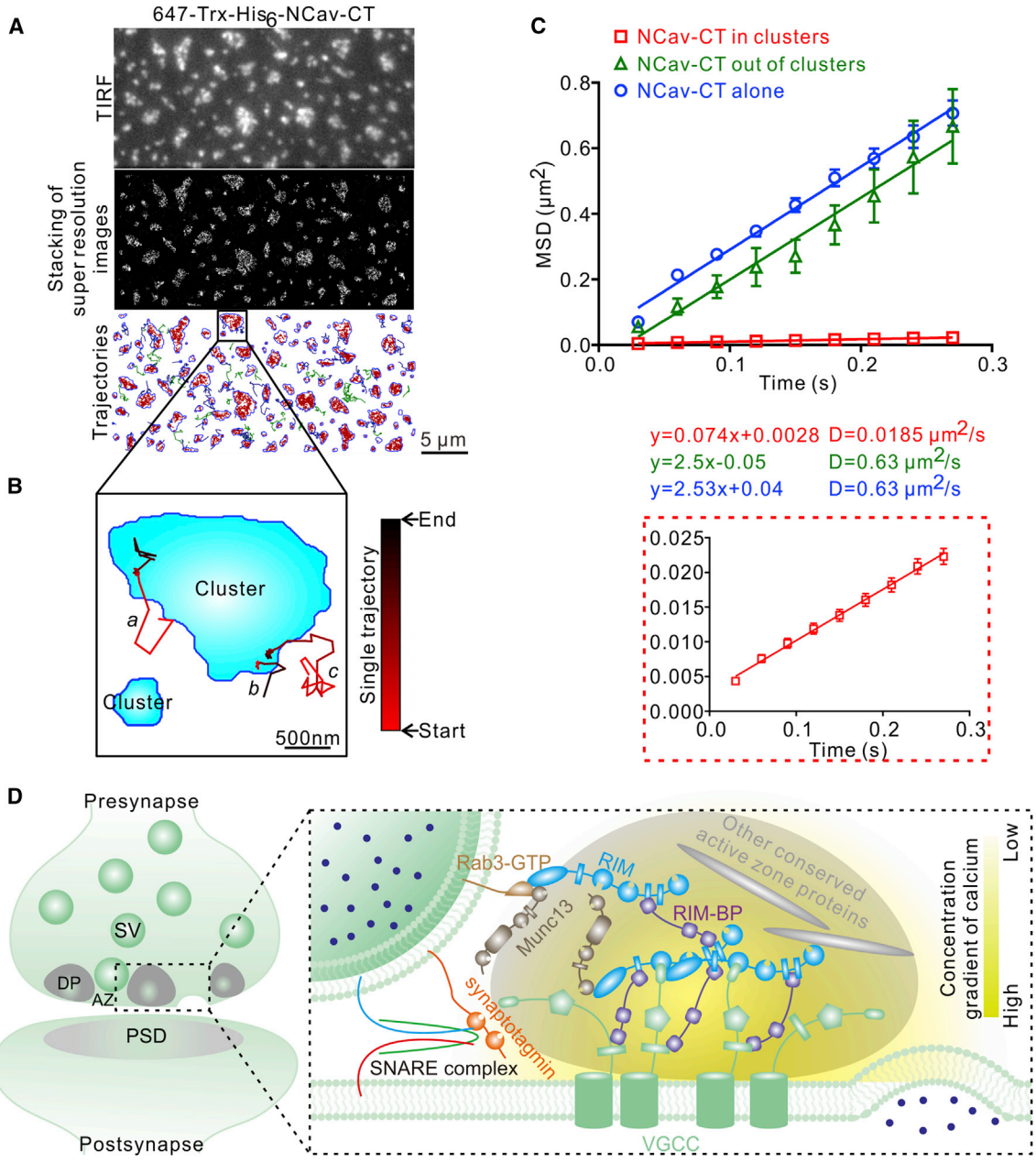

Figure 6. Super-resolution Imaging Indicates that Ca^{2+} Channels Are Clustered into Stable Microdomains on the SLB

(A) dSTORM-TIRF super-resolution imaging analysis of Trx-His_6-NCav-CT clusters on the SLB. The top panel shows a representative epifluorescence image captured under the TIRF angle. The middle panel shows stacking of 6,000 frames of dSTORM images of the corresponding field, and the bottom panel displays trajectories of molecules that lasted for more than 10 consecutive frames. Phase boundaries of each cluster are indicated by blue lines. Trajectories in the condensed clusters and in the dilute phase are colored in red and green, respectively. Trajectories that crossed the cluster boundaries are colored in deep blue.

(B) Representative trajectories showing individual Trx-His_6-NCav-CT molecules captured moving from the diluted phase into condensed phase that became trapped in the condensed phase (*a* and *c*). The trajectory *b* shows a Trx-His_6-NCav-CT molecule initially trapped in the condensed phase that later moved into the dilute phase and became more mobile. The motion directions are marked by gradient color from red to black.

(C) Determination of the diffusion coefficients of Trx-His_6-NCav-CT in the dilute and condensed phases formed by RIM1α-FL and RBP2-(SH3)3, as well as Trx-His_6-NCav-CT alone on the SLB. The diffusion coefficient (D) values are presented as mean ± SEM based on liner fitting of the curves. The number (n) of trajectories used for mean squared displacement (MSD) fitting was 2,664 for the molecules inside clusters, 37 for the molecules outside clusters, and 740 for trajectories of NCav-CT alone on the SLB.

(legend continued on next page)

Super-resolution Imaging Indicated Ca^{2+} Channels Were Clustered into Stable Microdomains on the SLB

We next used direct stochastic optical reconstruction microscopy (dSTORM) in total internal reflection fluorescence (TIRF) mode to characterize the properties of Trx-His_6-NCav-CT at the single-molecule level on the SLB. Alexa-Fluor-647-labeled Trx-His_6-NCav-CT was imaged and traced as a function of time. The reconstructed dSTORM images comprising 6,000 frames showed that the Trx-His_6-NCav-CT clusters could be very well aligned with the epifluorescence image of the corresponding region captured at the TIRF angle (Figure 6A). The dSTORM image also showed that the concentration of Trx-His_6-NCav-CT in condensed clusters is ~50-fold of that in the dilute phase. We were not able to quantify the concentration ratios for RIM1α-FL and RBP2-(SH3)3 on the SLB, as the molecules of both proteins moved out of the TIRF focal plane into dilute solution during the imaging process. Single-molecule trajectory tracking by dSTORM also revealed that Trx-His_6-NCav-CT was much more mobile in the dilute phase than in the condensed phase. Additionally, we could directly observe that Trx-His_6-NCav-CT moved from the dilute phase into the condensed phase and became trapped or less mobile (or vice versa) (Figure 6B). This single-molecule-based tracking also allowed us to measure the diffusion coefficient of Trx-His_6-NCav-CT on the SLB in both the condensed phase and the dilute phase (Figure 6C). Trx-His_6-NCav-CT alone or in the dilute phase displayed a similar diffusion coefficient of ~0.6 $\mu m^2/s$, and clustering of Trx-His_6-NCav-CT in the condensed phase decreased the diffusion coefficient to ~0.02 $\mu m^2/s$ (Figure 6C), revealing that the movements of NCav-CT were dramatically slowed down when trapped in the condensed phase. Taken together, the above super-resolution imaging experiments indicated that formation of the RIM, RIM-BP, and Trx-His_6-NCav-CT condensates not only concentrates Ca^{2+} channels but also assembles clustered Ca^{2+} channels into stable microdomains within subregions of membrane bilayers.

DISCUSSION

The highly specialized electron-dense active zone is responsible for synaptic vesicle tethering, docking, priming, fusion, and neurotransmitter release. Vast genetic screening and proteomic studies combined with physiological characterization have uncovered the molecular composition of the active zone and its individual role in these processes (Südhof, 2012), but exactly how each active zone is organized remains unclear due to its extreme complexity. Since the concept of LLPS came into sight in recent years (Brangwynne et al., 2009), it is increasingly recognized that phase separation may be a general strategy for cells to form membraneless subcellular compartments with broad physiological functions (Banani et al., 2017; Hyman et al., 2014; Shin and Brangwynne, 2017). Emerging evidence suggests that neurons also adopt the phase separation strategy to form subcellular compartments, including postsynaptic density (PSD) (Zeng et al., 2016, 2018) and synaptic vesicle clusters (Milovanovic et al., 2018). The formation of membraneless subcellular compartments like postsynaptic density signaling complexes via LLPS appears to be ideally suited for neurons due to their extreme morphologies and extraordinary levels of compartmentalization (Zeng et al., 2016, 2018). In this study, we provide evidence to show that the presynaptic active zone may also be formed through LLPS. Using an *in vitro* biochemical reconstitution approach, we demonstrate that RIM and RIM-BP, two major scaffold proteins in the active zone, can autonomously undergo LLPS and form highly condensed but dynamic compartments both in solution and on supported membrane bilayers. Importantly, the RIM and RIM-BP complex can effectively cluster the Ca^{2+} channel into microdomains. Based on the NCav-CT density measured on the supported membrane bilayer (Figure 5), we calculated that a dense projection-like structure may contain ~20 channels by naively assuming that each dense projection-like nanodomain has a diameter of ~50 nm (Zhai and Bellen, 2004). This estimated channel density is in the same order of that derived from EM-based measurements of neuronal synapses (Figure 6D) (Miki et al., 2017; Nakamura et al., 2015). Additionally, RIM is known to directly bind to Rab3 and Munc13 via its N-terminal zinc finger (Dulubova et al., 2005; Südhof, 2012). Therefore, the dense projection-like protein assembly formed by RIM, RIM-BP, and the Ca^{2+} channel could be directly coupled to the SNARE machinery and vesicle via Munc13 and Rab3 for fast and precise timing of neurotransmitter release (Eggermann et al., 2011) (Figure 6D). Thus, our study may have uncovered an underlying principle governing how presynaptic active zones form and function to regulate neurotransmitter release.

All synapses contain electron-dense active zones, though the morphology can be different in different types of neurons (Südhof, 2012). RIMs and RIM-BPs are the components essential for forming active zones, as simultaneous knockout of RIMs and RIM-BPs totally abolishes the dense projection structure (Acuna et al., 2016). We demonstrated in this work that the multivalent interactions between RIM and RIM-BP and the intrinsically disordered regions of both proteins are sufficient to form highly condensed and dynamic assemblies that are reminiscent of dense projection-like structures. It is important to note that the formation of active zones requires a number of other proteins in addition to RIM and RIM-BP. For example, it has recently been shown that double knockout of RIM and ELKS disrupted active zone formation and eliminated synaptic vesicle docking and Ca^{2+}-dependent synaptic transmission in neurons (Wang et al., 2016), indicating the critical role of ELKS together with RIM in the formation of active zones. A number of other proteins (e.g., liprins, CASK, Piccolo, and Bassoon) can directly or indirectly interact with the RIM, RIM-BP, and ELKS complex and thus further promote the valence and network complexity of active

(D) A model depicting clustering of VGCCs by the RIM and RIM-BP condensates and positioning of the clustered VGCCs in close proximity to the Ca^{2+} sensors (synaptotagmins) residing on the docked SNARE fusion machineries, ensuring spatiotemporal precision of neurotransmitter releases initiated by each action potential. The shaded gray sphere indicates the formation of dense projection-like structure via phase separation of the RIM, RIM-BP, and VGCC (and likely other active zone proteins not studied in the current work). The Ca^{2+} concentration gradient is indicated by a color gradient from yellow to white. AZ, active zone; DP, dense projection; PSD, postsynaptic density; SV, synaptic vesicle.

zone assembly (Südhof, 2012). For example, both liprin and ELKS have an N-terminal coiled-coil domain, which contributes to self-association of proteins and inter-molecular interactions (Ko et al., 2003). Therefore, both the morphology and Ca^{2+} channel clustering property of active zones in different neurons may be different due to their specific expressions of active zone proteins (or their isoforms) in addition to RIMs and RIM-BPs. The simple but defined biochemical reconstitution system using RIM, RIM-BP, and NCav-CT demonstrated here provides a starting point to investigate how other presynaptic active zone components, including proteins, membrane lipids, and other signaling molecules, may modulate the formation and dynamic regulation of active zones in nervous systems. Combined with further genetic and cell biology studies, this *in vitro* reconstitution approach may offer unique advantages in dissecting the roles of each individual component in active zone formation and function.

In summary, RIMs and RIM-BPs, two key scaffold proteins of active zones, can form self-organized, highly condensed but dynamic assemblies through LLPS. It is likely that other active zone proteins such as ELKs, liprins, Piccolo, and Bassoon function together with RIM and RIM-BP in a partially redundant fashion to organize the highly dense active zone protein assembly. The RIM and RIM-BP condensates can cluster VGCCs on the presynaptic plasma membranes. The RIM, RIM-BP, and VGCC condensates may recruit Munc13 via direct binding and dock vesicles to release sites. The positioning of clustered VGCCs in close proximity with the Ca^{2+} sensors residing on the SNARE fusion machinery supports spatiotemporal precision of neurotransmitter release initiated by each action potential.

STAR★METHODS

Detailed methods are provided in the online version of this paper and include the following:

- KEY RESOURCES TABLE
- CONTACT FOR REAGENT AND RESOURCE SHARING
- EXPERIMENTAL MODEL AND SUBJECT DETAILS
  - Bacterial strain
- METHOD DETAILS
  - Constructs and peptides
  - Protein expression and purification
  - Sortase-mediated protein ligation
  - Protein labeling with fluorophore
  - LLPS assays
  - Protein concentration measurements in the condensed phase
  - Preparation of supported lipid bilayers and LLPS on membrane
  - Fluorescence recovery after photobleaching (FRAP) assay
  - Estimation of absolute density on SLB
  - dSTORM imaging
  - Isothermal titration calorimetry (ITC) assay
  - Size exclusion chromatography coupled with multiangle light scattering (SEC-MALS) assay
- QUANTIFICATION AND STATISTICAL ANALYSIS
- DATA AND SOFTWARE AVAILABILITY

SUPPLEMENTAL INFORMATION

Supplemental Information includes six figures and two videos and can be found with this article online at https://doi.org/10.1016/j.molcel.2018.12.007.

ACKNOWLEDGMENTS

This work was supported by grants from the RGC of Hong Kong (AoE-M09-12 and C6004-17G) and a 973 program grant from the Minister of Science and Technology of China (2014CB910204) to M. Zhang and by a grant from HKUST (VPRGO12SC02) to S.D. M. Zhang is a Kerry Holdings Professor of Science and a Senior Fellow of IAS at HKUST.

AUTHOR CONTRIBUTIONS

X.W., Q.C., and Z.S. performed experiments; X.W., Q.C., Z.S., X.C., M. Zeng, S.D., and M. Zhang analyzed data; X.W., Q.C., and M. Zhang designed the research; X.W., Q.C., and M. Zhang drafted and all authors commented on the paper; and M. Zhang coordinated the project.

DECLARATION OF INTERESTS

The authors declare no competing interests.

Received: August 28, 2018
Revised: November 16, 2018
Accepted: December 11, 2018
Published: January 17, 2019

REFERENCES

Acuna, C., Liu, X., and Südhof, T.C. (2016). How to Make an Active Zone: Unexpected Universal Functional Redundancy between RIMs and RIM-BPs. Neuron *91*, 792–807.

Ball, L.J., Kühne, R., Schneider-Mergener, J., and Oschkinat, H. (2005). Recognition of proline-rich motifs by protein-protein-interaction domains. Angew. Chem. Int. Ed. Engl. *44*, 2852–2869.

Banani, S.F., Lee, H.O., Hyman, A.A., and Rosen, M.K. (2017). Biomolecular condensates: organizers of cellular biochemistry. Nat. Rev. Mol. Cell Biol. *18*, 285–298.

Banjade, S., and Rosen, M.K. (2014). Phase transitions of multivalent proteins can promote clustering of membrane receptors. eLife *3*, e04123.

Berry, J., Brangwynne, C.P., and Haataja, M. (2018). Physical principles of intracellular organization via active and passive phase transitions. Rep. Prog. Phys. *81*, 046601.

Betz, A., Thakur, P., Junge, H.J., Ashery, U., Rhee, J.S., Scheuss, V., Rosenmund, C., Rettig, J., and Brose, N. (2001). Functional interaction of the active zone proteins Munc13-1 and RIM1 in synaptic vesicle priming. Neuron *30*, 183–196.

Biederer, T., Kaeser, P.S., and Blanpied, T.A. (2017). Transcellular nanoalignment of synaptic function. Neuron *96*, 680–696.

Bloom, F.E., and Aghajanian, G.K. (1966). Cytochemistry of synapses: selective staining for electron microscopy. Science *154*, 1575–1577.

Brangwynne, C.P., Eckmann, C.R., Courson, D.S., Rybarska, A., Hoege, C., Gharakhani, J., Jülicher, F., and Hyman, A.A. (2009). Germline P granules are liquid droplets that localize by controlled dissolution/condensation. Science *324*, 1729–1732.

Couteaux, R., and Pécot-Dechavassine, M. (1970). [Synaptic vesicles and pouches at the level of "active zones" of the neuromuscular junction]. C. R. Acad. Sci. Hebd. Seances Acad. Sci. D *271*, 2346–2349.

de Jong, A.P.H., Roggero, C.M., Ho, M.R., Wong, M.Y., Brautigam, C.A., Rizo, J., and Kaeser, P.S. (2018). RIM C2B domains target presynaptic active zone functions to PIP2-containing membranes. Neuron *98*, 335–349.e337.

Dulubova, I., Lou, X., Lu, J., Huryeva, I., Alam, A., Schneggenburger, R., Südhof, T.C., and Rizo, J. (2005). A Munc13/RIM/Rab3 tripartite complex: from priming to plasticity? EMBO J. *24*, 2839–2850.

Eggermann, E., Bucurenciu, I., Goswami, S.P., and Jonas, P. (2011). Nanodomain coupling between Ca^{2+} channels and sensors of exocytosis at fast mammalian synapses. Nat. Rev. Neurosci. *13*, 7–21.

Gray, E.G. (1975). Synaptic fine structure and nuclear, cytoplasmic and extracellular networks: The stereoframework concept. J. Neurocytol. *4*, 315–339.

Gray, E.G., and Guillery, R.W. (1966). Synaptic morphology in the normal and degenerating nervous system. Int. Rev. Cytol. *19*, 111–182.

Guan, R., Dai, H., Tomchick, D.R., Dulubova, I., Machius, M., Südhof, T.C., and Rizo, J. (2007). Crystal structure of the RIM1alpha C2B domain at 1.7 A resolution. Biochemistry *46*, 8988–8998.

Hibino, H., Pironkova, R., Onwumere, O., Vologodskaia, M., Hudspeth, A.J., and Lesage, F. (2002). RIM binding proteins (RBPs) couple Rab3-interacting molecules (RIMs) to voltage-gated Ca(2+) channels. Neuron *34*, 411–423.

Hyman, A.A., Weber, C.A., and Jülicher, F. (2014). Liquid-liquid phase separation in biology. Annu. Rev. Cell Dev. Biol. *30*, 39–58.

Kaeser, P.S., Deng, L., Wang, Y., Dulubova, I., Liu, X., Rizo, J., and Südhof, T.C. (2011). RIM proteins tether Ca2+ channels to presynaptic active zones via a direct PDZ-domain interaction. Cell *144*, 282–295.

Ko, J., Na, M., Kim, S., Lee, J.R., and Kim, E. (2003). Interaction of the ERC family of RIM-binding proteins with the liprin-alpha family of multidomain proteins. J. Biol. Chem. *278*, 42377–42385.

Kucerka, N., Tristram-Nagle, S., and Nagle, J.F. (2005). Structure of fully hydrated fluid phase lipid bilayers with monounsaturated chains. J. Membr. Biol. *208*, 193–202.

Li, P., Banjade, S., Cheng, H.C., Kim, S., Chen, B., Guo, L., Llaguno, M., Hollingsworth, J.V., King, D.S., Banani, S.F., et al. (2012). Phase transitions in the assembly of multivalent signalling proteins. Nature *483*, 336–340.

Ma, C., Li, W., Xu, Y., and Rizo, J. (2011). Munc13 mediates the transition from the closed syntaxin-Munc18 complex to the SNARE complex. Nat. Struct. Mol. Biol. *18*, 542–549.

Manley, S., Gillette, J.M., Patterson, G.H., Shroff, H., Hess, H.F., Betzig, E., and Lippincott-Schwartz, J. (2008). High-density mapping of single-molecule trajectories with photoactivated localization microscopy. Nat. Methods *5*, 155–157.

Maschi, D., and Klyachko, V.A. (2017). Spatiotemporal regulation of synaptic vesicle fusion sites in central synapses. Neuron *94*, 65–73.e63.

Miki, T., Kaufmann, W.A., Malagon, G., Gomez, L., Tabuchi, K., Watanabe, M., Shigemoto, R., and Marty, A. (2017). Numbers of presynaptic Ca^{2+} channel clusters match those of functionally defined vesicular docking sites in single central synapses. Proc. Natl. Acad. Sci. USA *114*, E5246–E5255.

Milovanovic, D., Wu, Y., Bian, X., and De Camilli, P. (2018). A liquid phase of synapsin and lipid vesicles. Science *361*, 604–607.

Nakamura, Y., Harada, H., Kamasawa, N., Matsui, K., Rothman, J.S., Shigemoto, R., Silver, R.A., DiGregorio, D.A., and Takahashi, T. (2015). Nanoscale distribution of presynaptic Ca(2+) channels and its impact on vesicular release during development. Neuron *85*, 145–158.

Park, H., Li, Y., and Tsien, R.W. (2012). Influence of synaptic vesicle position on release probability and exocytotic fusion mode. Science *335*, 1362–1366.

Pfenninger, K., Akert, K., Moor, H., and Sandri, C. (1972). The fine structure of freeze-fractured presynaptic membranes. J. Neurocytol. *1*, 129–149.

Popp, M.W., and Ploegh, H.L. (2011). Making and breaking peptide bonds: protein engineering using sortase. Angew. Chem. Int. Ed. Engl. *50*, 5024–5032.

Richmond, J.E., Weimer, R.M., and Jorgensen, E.M. (2001). An open form of syntaxin bypasses the requirement for UNC-13 in vesicle priming. Nature *412*, 338–341.

Schoch, S., Castillo, P.E., Jo, T., Mukherjee, K., Geppert, M., Wang, Y., Schmitz, F., Malenka, R.C., and Südhof, T.C. (2002). RIM1alpha forms a protein scaffold for regulating neurotransmitter release at the active zone. Nature *415*, 321–326.

Shin, Y., and Brangwynne, C.P. (2017). Liquid phase condensation in cell physiology and disease. Science *357*, eaaf4382.

Siksou, L., Varoqueaux, F., Pascual, O., Triller, A., Brose, N., and Marty, S. (2009). A common molecular basis for membrane docking and functional priming of synaptic vesicles. Eur. J. Neurosci. *30*, 49–56.

Südhof, T.C. (2012). The presynaptic active zone. Neuron *75*, 11–25.

Tang, A.H., Chen, H., Li, T.P., Metzbower, S.R., MacGillavry, H.D., and Blanpied, T.A. (2016). A trans-synaptic nanocolumn aligns neurotransmitter release to receptors. Nature *536*, 210–214.

Theillet, F.X., Kalmar, L., Tompa, P., Han, K.H., Selenko, P., Dunker, A.K., Daughdrill, G.W., and Uversky, V.N. (2013). The alphabet of intrinsic disorder: I. Act like a pro: on the abundance and roles of proline residues in intrinsically disordered proteins. Intrinsically Disord. Proteins *1*, e24360.

Wang, Y., Sugita, S., and Sudhof, T.C. (2000). The RIM/NIM family of neuronal C2 domain proteins. Interactions with Rab3 and a new class of Src homology 3 domain proteins. J. Biol. Chem. *275*, 20033–20044.

Wang, S.S.H., Held, R.G., Wong, M.Y., Liu, C., Karakhanyan, A., and Kaeser, P.S. (2016). Fusion competent synaptic vesicles persist upon active zone disruption and loss of vesicle docking. Neuron *91*, 777–791.

Watanabe, S., Rost, B.R., Camacho-Pérez, M., Davis, M.W., Söhl-Kielczynski, B., Rosenmund, C., and Jorgensen, E.M. (2013). Ultrafast endocytosis at mouse hippocampal synapses. Nature *504*, 242–247.

Wilhelm, B.G., Mandad, S., Truckenbrodt, S., Kröhnert, K., Schäfer, C., Rammner, B., Koo, S.J., Claßen, G.A., Krauss, M., Haucke, V., et al. (2014). Composition of isolated synaptic boutons reveals the amounts of vesicle trafficking proteins. Science *344*, 1023–1028.

Yang, X., Wang, S., Sheng, Y., Zhang, M., Zou, W., Wu, L., Kang, L., Rizo, J., Zhang, R., Xu, T., and Ma, C. (2015). Syntaxin opening by the MUN domain underlies the function of Munc13 in synaptic-vesicle priming. Nat. Struct. Mol. Biol. *22*, 547–554.

Zeng, M., Shang, Y., Araki, Y., Guo, T., Huganir, R.L., and Zhang, M. (2016). Phase transition in postsynaptic densities underlies formation of synaptic complexes and synaptic plasticity. Cell *166*, 1163–1175.e1112.

Zeng, M., Chen, X., Guan, D., Xu, J., Wu, H., Tong, P., and Zhang, M. (2018). Reconstituted postsynaptic density as a molecular platform for understanding synapse formation and plasticity. Cell *174*, 1172–1187.e16.

Zhai, R.G., and Bellen, H.J. (2004). The architecture of the active zone in the presynaptic nerve terminal. Physiology (Bethesda) *19*, 262–270.

Zhao, T., Wang, Y., Zhai, Y., Qu, X., Cheng, A., Du, S., and Loy, M.M. (2015). A user-friendly two-color super-resolution localization microscope. Opt. Express *23*, 1879–1887.

STAR★METHODS

KEY RESOURCES TABLE

REAGENT or RESOURCE	SOURCE	IDENTIFIER
Chemicals, Peptides, and Recombinant Proteins		
Chemical: iFluor 488 NHS Ester	AAT Bioquest	Cat# 1023
Chemical: Cy3 NHS Ester	AAT Bioquest	Cat# 271
Chemical: Cy5 NHS Ester	AAT Bioquest	Cat# 280
Chemical: Alexa Fluor 647 NHS Ester	Thermo Fisher	Cat# A20106
Chemical: 16:0-18:1 PC	Avanti Polar Lipids	Cat# 850457C
Chemical: 18:1 DGS-NTA(Ni)	Avanti Polar Lipids	Cat# 790404C
Chemical: 18:1 PEG5000 PE	Avanti Polar Lipids	Cat# 880230C
Chemical: 18:1 Cy5 PE	Avanti Polar Lipids	Cat# 810335C
Peptide: RIM1α-PRM (RRGRQLPQVPVRSGS)	China Peptide	N/A
Peptide: RIM1α-PRM2 (QPSPFMPRRHIHGE)	China Peptide	N/A
Peptide: NCav-PBM (HPDQDHWC)	China Peptide	N/A
Recombinant protein: RIM1α-PAS (aa 481-1097)	This paper	N/A (custom-made)
Recombinant protein: RIM1α-PASΔPRM1 (aa 481-501+511-1097)	This paper	N/A (custom-made)
Recombinant protein: RIM1α-PASΔPRM2 (aa 481-572+877-1097)	This paper	N/A (custom-made)
Recombinant protein: RIM1α-PASΔPRM (aa 481-1085+1090-1097)	This paper	N/A (custom-made)
Recombinant protein: RIM1α-PDZ (aa 481-709)	This paper	N/A (custom-made)
Recombinant protein: RIM1α-AS (aa 710-1097)	This paper	N/A (custom-made)
Recombinant protein: RIM1α-A (aa 710-870)	This paper	N/A (custom-made)
Recombinant protein: RIM1α-S (aa 871-1097)	This paper	N/A (custom-made)
Recombinant protein: RIM1α-SΔ10 (aa 881-1097)	This paper	N/A (custom-made)
Recombinant protein: RIM1α-PRM (aa 1061-1097)	This paper	N/A (custom-made)
Recombinant protein: RIM1α-PRM2 (aa 871-880)	This paper	N/A (custom-made)
Recombinant protein: RIM1α-PRM1 (aa 481-524)	This paper	N/A (custom-made)
Recombinant protein: RIM1α-N-LPETGG (aa 1-474-LPETGG)	This paper	N/A (custom-made)
Recombinant protein: RIM1α-PASB (aa 481-1334)	This paper	N/A (custom-made)
Recombinant protein: Sortase A-ΔN59 (aa 60-206)	Popp and Ploegh, 2011	
Recombinant protein: RIM1α-FL (aa 1-1334)	This paper	N/A (custom-made)
Recombinant protein: RIM1α-N (aa 1-480)	This paper	N/A (custom-made)
Recombinant protein: RIM1α-ZF (aa 1-182)	This paper	N/A (custom-made)
Recombinant protein: RIM1α-Nlinker (aa 183-480)	This paper	N/A (custom-made)
Recombinant protein: RBP2-(SH3)3 (aa 178-252+844-1040)	This paper	N/A (custom-made)
Recombinant protein: RBP2-1st SH3 (aa 178-252)	This paper	N/A (custom-made)
Recombinant protein: RBP2-2nd SH3 (aa 844-965)	This paper	N/A (custom-made)
Recombinant protein: RBP2-3rd SH3 (aa 966-1040)	This paper	N/A (custom-made)
Recombinant protein: NCav-CT (aa 2151-2327)	This paper	N/A (custom-made)
Recombinant protein: NCav-CTΔPRM (aa 2151-2178+2183-2327)	This paper	N/A (custom-made)
Recombinant protein: NCav-CTΔPNGY (aa 2151-2298+2303-2327)	This paper	N/A (custom-made)
Recombinant protein: NCav-CTΔPRM (aa 2151-2323)	This paper	N/A (custom-made)
Recombinant protein: PSD95-FL (aa 1-724)	Zeng et al., 2016	
Recombinant protein: SynGAP-CC-PBM (aa 1147-1308)	Zeng et al., 2016	
Experimental Models: Organisms/Strains		
Escherichia coli BL21 (DE3) cells	Invitrogen	Cat# C600003

(*Continued on next page*)

Continued

REAGENT or RESOURCE	SOURCE	IDENTIFIER
Recombinant DNA		
32m3c-RIM1α-PAS	This paper	N/A (custom-made)
32m3c-RIM1α-PASΔPRM1	This paper	N/A (custom-made)
32m3c-RIM1α-PASΔPRM2	This paper	N/A (custom-made)
32m3c-RIM1α-PASΔPRM	This paper	N/A (custom-made)
32m3c-RIM1α-PDZ	This paper	N/A (custom-made)
32m3c-RIM1α-AS	This paper	N/A (custom-made)
32m3c-RIM1α-A	This paper	N/A (custom-made)
32m3c-RIM1α-S	This paper	N/A (custom-made)
32m3c-RIM1α-SΔ10	This paper	N/A (custom-made)
32m3c-RIM1α-PRM	This paper	N/A (custom-made)
32m3c-RIM1α-PRM2	This paper	N/A (custom-made)
32m3c-RIM1α-PRM1	This paper	N/A (custom-made)
32m3c-RIM1α-N-LPETGG	This paper	N/A (custom-made)
32mTEV-RIM1α-PASB	This paper	N/A (custom-made)
Sortase A-ΔN59	Popp and Ploegh, 2011	
32m3c-RIM1α-N	This paper	N/A (custom-made)
32m3c-RIM1α-ZF	This paper	N/A (custom-made)
32m3c-RIM1α-Nlinker	This paper	N/A (custom-made)
m3c-RBP2-(SH3)3	This paper	N/A (custom-made)
32m3c-RBP2-1st SH3	This paper	N/A (custom-made)
32m3c-RBP2-2nd SH3	This paper	N/A (custom-made)
32m3c-RBP2-3rd SH3	This paper	N/A (custom-made)
32m3c-NCav-CT	This paper	N/A (custom-made)
32mTEV-NCav-CT	This paper	N/A (custom-made)
32m3c-NCav-CTΔPRM	This paper	N/A (custom-made)
32m3c-NCav-CTΔPNGY	This paper	N/A (custom-made)
32m3c-NCav-CTΔPRM	This paper	N/A (custom-made)
32m3c-PSD95-FL	Zeng et al., 2016	
32m3c-SynGAP-CC-PBM	Zeng et al., 2016	
Software and Algorithms		
Origin 7.0	OriginLab	https://www.originlab.com/
ASTRA 6	Wyatt	https://www.wyatt.com/products/software/astra.html
ImageJ	NIH	https://imagej.nih.gov/ij/
Prism	GraphPad	https://www.graphpad.com/scientific-software/prism/
Amino Acid Composition Analysis	This paper	http://qxcai.people.ust.hk/aaca.html

CONTACT FOR REAGENT AND RESOURCE SHARING

Further information and requests for resources and reagents should be directed to and will be fulfilled by the Lead Contact, Mingjie Zhang (mzhang@ust.hk).

EXPERIMENTAL MODEL AND SUBJECT DETAILS

Bacterial strain

Escherichia coli BL21(DE3) cells were used in this study for the production of recombinant proteins. Cells were cultured in LB medium supplemented with necessary antibiotics.

METHOD DETAILS

Constructs and peptides

Rat RIM1α (GenBank: XM_017596673.1) and RIM-BP2 (GenBank: XM_017598284.1) plasmids were kind gifts from Dr. Pascal S. Kaeser at Harvard Medical School. Various fragments of RIM1α were amplified by standard PCR method and inserted into a modified pET-32a vectors with a N-terminal Trx-His_6 tag and an HRV-3C protease cutting site or a TEV protease cutting site. The first SH3 domain were fused with the C-terminal SH3 tandem of RIM-BP2 by the overlap-extension PCR method and cloned into a vector with N-terminal His_6-tag and an HRV-3C protease cutting site. Cytoplasmic tail of N-type VGCC α1 subunit was amplified from a mouse brain cDNA library and cloned into the modified pET-32a vectors with a N-terminal Trx-His_6 tag and an HRV-3C protease cutting site. His_6-tagged sortase Δ59 plasmid was a kind gift from Dr. Xuewu Zhang in UT Southwestern Medical Center. All constructs were confirmed by DNA sequencing.

Three peptides, RIM1α-PRM (sequence: RRGRQLPQVPVRSGS), RIM1α-PRM2 (sequence: QPSPFMPRRHIHGE), and NCav-PBM (sequence: HPDQDHWC), were commercially synthesized by ChinaPeptides (Shanghai, China) with purity > 95%.

Protein expression and purification

All proteins were expressed in *Escherichia coli* BL21(DE3) cells (Agilent Technologies) in LB medium at 16°C. Recombinant proteins were purified using Ni^{2+}-NTA affinity column followed by a Superdex 200 26/60 size exclusion chromatography. The affinity tag of each protein was cleaved by HRV-3C protease or TEV protease at 4°C overnight and removed by another step of Superdex 200 26/60 size exclusion chromatography with a buffer containing 50 mM Tris pH 8.2, 200 mM NaCl, 1 mM EDTA and 1 mM DTT.

Sortase-mediated protein ligation

Purified RIM1α-N(1-474) with a "LPETGG"-tag at the C terminus (termed "RIM1α-N-LPETGG"; Figure S3A), GGG-RIM1α-PASB and sortase Δ59 were mixed at a 2:1:1 molar ratio. The ligation reaction was initiated by addition of 10 mM $CaCl_2$ at room temperature for 2 h. The ligated RIM1α-FL was separated from unreacted mixtures by Superdex 200 26/60 size exclusion chromatography in a buffer containing 50 mM Tris pH 8.2, 300 mM NaCl, 1 mM EDTA and 1 mM DTT.

Protein labeling with fluorophore

The fluorophores, including iFluor 488/Cy3/Cy5 NHS ester (AAT Bioquest) and Alexa 647 NHS ester (ThermoFisher), were dissolved in DMSO. Purified proteins were exchanged to a buffer containing 100 mM $NaHCO_3$, pH 8.3, 200 mM NaCl, 1 mM EDTA and 1 mM DTT using a HiTrap desalting column. The fluorophores were added into protein solution in 1:1 molar ratio and the mixture was incubated at room temperate for 1 h. After quenched by 200 mM Tris pH 8.2, labeled protein was exchanged into buffer containing 50 mM Tris pH 8.2, 200 mM NaCl, 1 mM EDTA and 1 mM DTT using a HiTrap desalting column. Fluorescence labeling efficiency was detected using Nanodrop 2000 (ThermoFisher).

LLPS assays

All purified proteins were centrifuged at 16,873 g in 4°C for 10 min to remove potential aggregates and precipitations prior to LLPS assays. Proteins were directly mixed to reach specified concentrations. The final buffer of LLPS assay mixtures was 50 mM Tris pH 8.2, 200 mM NaCl, 1 mM EDTA and 5 mM DTT.

For sedimentation-based assays, the total volume of each mixture is 50 μL. After incubation at room temperature for 10 min, the mixture was centrifuged at 16,873 g at 22°C for 5 min. The supernatant was collected, and the pellet was washed with 50 μL of the same buffer and then thoroughly resuspended with 50 μL buffer. Samples from supernatant fraction and pellet fraction were analyzed by SDS-PAGE with Coomassie blue R250 staining. Three repeats were performed for each group. The intensity of each band on SDS-PAGE was quantified by ImageJ and data were presented as mean ± SD.

For microscope-based assay, each mixture was injected into a home-made chamber composed of a coverslip and a glass slide assembled with one layer of double-sided tape. DIC images and fluorescent images were captured using a Nikon Ni-U upright fluorescence microscope at room temperature.

Protein concentration measurements in the condensed phase

Each protein was first labeled with Cy3 and then diluted with unlabeled protein to reach the final labeling ratio of 1%. For each experiment, only one protein was labeled while the rest were unlabeled to prevent any potential signal cross-talk. Proteins were mixed to a final concentration of 10 μM and injected into a homemade chamber. Samples containing condensed droplets were and imaged by Zeiss LSM880 confocal microscopy with a 63 × objective lens in a z stack mode. Pinhole size was set at 0.9 μm and the z stack step interval was 1.0 μm. The lowest z-slice started with the focus in the coverslip layer and the highest z-slice ended with the focus entering the dilute solution layer. Identical parameters (including laser power, detector gain, resolution, scanning speed, etc.) were used during the imaging processes. To assure system stability, all measurements, together with the calibration curve, were completed in one single imaging session.

Images were analyzed with ImageJ. For quantification, we define that a z-slice with its peak intensity < 10% deviation from the maximal peak intensity layer (i.e., $(I_{max}\text{-}I)/I_{max} < 10\%$) is with its imaging plane point spread function entirely within the z-dimension

of the droplet (Figure S6B). We selected droplets with height larger than 5 μm for quantifications, so that more than two such layers can be used for quantitative analysis. The fluorescence intensities of the layers within one droplet that satisfy the $(I_{max}-I)/I_{max} < 10\%$ criteria were averaged for absolute protein concentration calculation. Eight droplets were quantified to derive the concentration of each molecule in the condensed phase. For the standard curve, indicated concentrations of Cy3 labeled RBP2-(SH3)3 were measured at the same setting (Figure 6C). With this standard curve, the measured fluorescence intensity for each component in a given condensed phase could be converted into absolute molar concentration. Measured results were expressed as mean ± SD.

Preparation of supported lipid bilayers and LLPS on membrane

The preparation of supported lipid bilayers (SLB) followed the method described in a previous study (Banjade and Rosen, 2014) with modifications. Specifically, lipids comprising 98% POPC, 2% DGS-NTA(Ni) and 0.1% PEG5000 PE (all lipids were purchased from Avantilipids and dissolved in chloroform, Lot No. 850457, 790404, 880230) were dried under a stream of nitrogen gas and resuspended by PBS buffer to generate a multi-lamellar vesicle solution with a final concentration of 0.5 mg/mL. After hydration and overnight aging at 4°C, small uni-lamellar vesicles (SUV) were generated through repeatedly freezing and thaw in combination with sonication in a 37°C water bath until the solution turned clear. The lipid solution was then centrifuged at 33,500 g for 45 min at 4°C and the supernatant containing SUV was kept for further use.

Chambered cover glass (Lab-tek) was initially washed with Hellmanex II (Hëlma Analytics) overnight, thoroughly rinsed with MilliQ water. The cover glass was then washed with 5 M NaOH for 1 h at 50°C and thoroughly rinsed with MilliQ water, and this process was repeated three times. The cleaned cover glass was then equilibrated with PBS buffer, followed by addition of 150 μL SUVs and incubation at 42°C for 1 h to generate SLB. SLB were washed with the reaction buffer containing 50 mM Tris pH 8.2, 200 mM NaCl, 1 mM TCEP for three times (6-fold dilution per time). It should be noted that SLB should not be exposed to the atmosphere to prevent oxidations. Then SLB were blocked with 1 mg/mL BSA in the reaction buffer at room temperature for 30 min.

All proteins used for LLPS on SLB were exchanged into the reaction buffer using a HiTrap desalting column. First, 500 nM 2% iFluor-488 labeled Trx-His_6-NCav-CT was incubated with SLB at room temperature for 1 h. Then the chamber was washed with 1 mg/mL BSA solution in the reaction buffer to remove unbound Trx-His_6-NCav-CT. Different concentrations of RIM1α-FL and RBP2-(SH3)3 were then added to Trx-His_6-NCav-CT coated SLB to induce LLPS.

Fluorescence recovery after photobleaching (FRAP) assay

FRAP experiments were carried out on a Zeiss LSM 880 confocal microscope at room temperature. Considering the size of the droplets, different lenses and regions of interest (ROI) were chosen for FRAP experiments in solution or on SLB. Specifically, 20 × lens with 2 × zoom in and a square region with the side length of 50 pixels (20.76 μm) was performed for FRAP in 3D solution, while 63 × oil lens with 4x zoom in and a square region with the side length of 30 pixels (1.98 μm) was performed for FRAP on SLB. In each FRAP experiment, fluorescence intensities of a neighboring droplet with similar size to the one used for photobleaching was recorded for fluorescence intensity correction and a third region in the background with the same size was also recorded for background signal subtraction. Cy3 or iFluor-488 labeled proteins were photobleached by 561 nm or 488 nm laser beams at 100% power respectively. Each data point represented the averaged signal of three droplets in solution or of three clustered areas on the SLB with similar sizes. All experiments were completed within 2 h after initiation of the phase separations. For data analysis, the intensity at the pre-bleach point was normalized to 100%, and the intensity right after the bleaching was set to 0%. Data were expressed as mean ± SD.

Estimation of absolute density on SLB

The density of Trx-His_6-NCav-CT on the SLB was quantified based on fluorescence intensity. First, SUVs with Cy5 labeled PE (Avantilipids, Lot No. 810335) combined in different ratios from $(1/128)\%$ to $(1/4)\%$ were prepared to make SLB as described above. Cy5 PE was evenly distributed on SLB (Figure 5A). Assuming the surface area of lipid head group is 69 $Å^2$ (Kucerka et al., 2005), the corresponding densities of Cy5 PE were 22.64 to 724.64 molecules per μm^2. Confocal images were captured by Zeiss LSM880 confocal microscopy with a 63 × objective lens. Pinhole size was set at 0.9 μm. A linear regulation fitting was analyzed to obtain a standard curve of fluorescence intensity versus Cy5 PE density (Figure 5B).

Second, the same setting (including laser power, detector gain, resolution, scanning speed, etc.) was used for the 2% Cy5 labeled Trx-His_6-NCav-CT clusters imaging. It was noticed that the fluorescent intensity inside the clusters were nearly the same in a given condition (Figure 5C), allowing us to further average multiple clusters for quantification. Considering the size difference caused by different concentration of RIM and RIM-BP, we set a size threshold of 0.1 μm^2 to include various size. Intensities of fifteen clusters from five independent images of each condition were measured and expressed as mean ± SD (Figure 5D).

It is supposed that the same fluorophore conjugated to lipid or protein share the same illuminating property. So the absolute density of Cy5 labeled Trx-His_6-NCav-CT can be calculated based on the standard curve generated by Cy5 PE, and therefore the exact number of calcium channel in a given area, for example, the active zone, can be estimated.

dSTORM imaging

All the pre-imaging processes were the same as LLPS on SLB as described above. Before imaging, fresh imaging buffer (the reaction buffer containing 10% D-Glucose (Sigma G8270, 5 × stock prepared in the reaction buffer), 0.56 mg/mL Glucose Oxidase (Sigma G2133-50KU, 100 × stock prepared in the reaction buffer), 0.04 mg/mL Catalase (Sigma C9322-10G, 100 × stock prepared in the

reaction buffer) and 30 mM β-mercaptoethanol) was injected into the chamber to replace the original reaction buffer. Imaging of each well was completed within half an hour upon addition of imaging buffer.

Supper-resolution images were taken by a custom-built dSTORM with two channels based on a Nikon Ti-E inverted microscope (Zhao et al., 2015). Here we only used one channel for samples labeled with Alexa 647. A 100 × objective lens (CFI Apo TIRFM 100x Oil, N.A. 1.49, Nikon) was used to observe the fluorescence signals. An EMCCD (electron-multiplying charge-coupled device, Andor, IXon-Ultra) was applied to collect the emission lights that passed through a channel splitter. For each sample, 50 frames of TIRF images were captured first with an exposure time of 30 ms/frame. Then the sample was subjected to a 30 s bleaching followed by capturing 6000 frames of images under super-resolution mode with an exposure time of 30 ms/frame. The laser intensity was fixed at 4.0 kW/cm^2 during the 30 s bleaching and the super-resolution imaging and the microscope was at the TIRF mode. The dSTORM-TIRF raw images were processed by Rohdea (Nanobioimaging Ltd., Hong Kong) and reconstructed by ImageJ.

Estimation of enrichment of each component into the condensed phase was based on detected molecules/fluorophore locations within a unit region (defined as local density within a circle with the diameter of 200 nm) in the condensed and dilute phases by dSTORM images. An average local density was defined as: (total number of locations in an imaging field / total area of the field) × area of each unit region. A condensed phase region was defined when its density was higher than the average local density, and a dilute phase region was defined when its density was lower than the average local density. The ratio of location density of the condensed phase to that of the dilute phase was defined as the fold of component enrichment via LLPS.

For single molecule tracking analysis, two signals/locations with a distance < 500 nm in two consecutive frames was assigned to originate from a same molecule. If there are multiple locations within this 500 nm diameter zone, the two locations with the shortest distance were considered as two consecutive trajectories of one molecule (Manley et al., 2008). The diffusion coefficients of each NCav-CT in condensed and dilute phases were obtained by calculating the mean squared displacement (MSD) for trajectories lasted for > 10 frames in each phase. Assuming that each NCav-CT molecule was restricted on a two-dimensional membrane on SLB, its MSD as the function of time should follow the equation: $MSD = 4Dt + C$, where D is diffusion coefficient and the C is a constant.

Isothermal titration calorimetry (ITC) assay

ITC experiments were performed using a MicroCal VP-ITC calorimeter (Malvern) at 25°C. All proteins or peptides used in ITC experiments were exchanged to the binding buffer containing 50 mM Tirs pH 8.2, 200 mM NaCl, 1 mM EDTA and 1 mM DTT. Each titration point was performed by injecting a 10 μL aliquot of one protein in the syringe into its binding protein in the cell at a time interval of 120 s to ensure that the titration peak returned to the baseline. Titration data were fitted with the one-site binding model using Origin 7.0.

Size exclusion chromatography coupled with multiangle light scattering (SEC-MALS) assay

This series of experiments were performed on an AKTA purifier system (GE Healthcare) coupled with a static light scattering detector (miniDawn, Wyatt) and a differential refractive index detector (Optilab, Wyatt). Protein samples (concentrations for each reaction were indicated in the figure legends) were filtered and loaded into a Superose 6 10/300 GL column or a Superose 12 10/300 GL column pre-equilibrated by a column buffer composed of 50 mM Tris pH 8.2, 200 mM NaCl, 1 mM EDTA, and 1 mM DTT. Data were analyzed using ASTRA6 (Wyatt).

QUANTIFICATION AND STATISTICAL ANALYSIS

Statistical parameters including the definitions and exact values of n (e.g., number of experiments, number of droplets, etc), distributions and deviations are reported in the Figures and corresponding Figure Legends. Data of *in vitro* LLPS sedimentation-based assay and FRAP assay were expressed as mean ± SD. ns, not significant; *, $p < 0.05$; **, $p < 0.01$; ***, $p < 0.001$; ****, $p < 0.0001$ using one-way ANOVA with Dunnett's multiple comparisons test. Statistical analysis was performed in GraphPad Prism.

DATA AND SOFTWARE AVAILABILITY

No data deposition is required for this study.